



**HAL**  
open science

# Compressibility-induced destabilisation of falling liquid films: an integral approach

P. Botticini, Gianluca Lavalle, D. Picchi, P. Poesio

► **To cite this version:**

P. Botticini, Gianluca Lavalle, D. Picchi, P. Poesio. Compressibility-induced destabilisation of falling liquid films: an integral approach. *International Journal of Multiphase Flow*, 2024, 171, pp.104667. 10.1016/j.ijmultiphaseflow.2023.104667 . emse-04302161

**HAL Id: emse-04302161**

**<https://hal-emse.ccsd.cnrs.fr/emse-04302161>**

Submitted on 22 Feb 2024

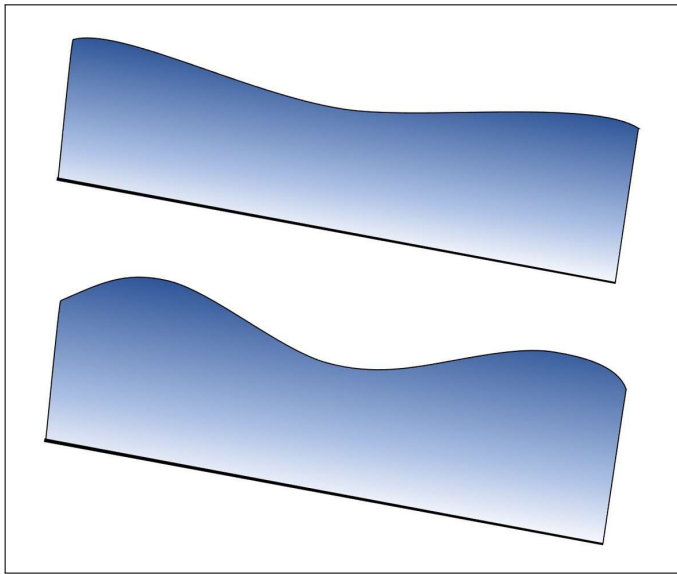
**HAL** is a multi-disciplinary open access archive for the deposit and dissemination of scientific research documents, whether they are published or not. The documents may come from teaching and research institutions in France or abroad, or from public or private research centers.

L'archive ouverte pluridisciplinaire **HAL**, est destinée au dépôt et à la diffusion de documents scientifiques de niveau recherche, publiés ou non, émanant des établissements d'enseignement et de recherche français ou étrangers, des laboratoires publics ou privés.

# Graphical Abstract

## Compressibility-induced destabilisation of falling liquid films: an integral approach

P. Botticini, G. Lavallo, D. Picchi, P. Poesio



## Highlights

### **Compressibility–induced destabilisation of falling liquid films: an integral approach**

P. Botticini, G. Lavallo, D. Picchi, P. Poesio

- We introduced small density variations within a gravity–driven falling film via a barotropic equation of state and investigated how this affects the flow temporal linear stability.
- In the final depth–averaged evolution equations compressibility is reflected in two additional second–order terms.
- A weak compressibility boosts the onset of interfacial instability, especially in low–inertial regimes and along modest slopes.
- We detected an extra flow rate of hydrostatic origin due to compressibility and complemented our analysis with the wave–hierarchy theory.

# Compressibility–induced destabilisation of falling liquid films: an integral approach

P. Botticini<sup>a,b</sup>, G. Lavallo<sup>a,\*</sup>, D. Picchi<sup>b</sup>, P. Poesio<sup>b</sup>

<sup>a</sup>*Mines Saint–Etienne, Univ. Lyon, CNRS, UMR 5307 LGF, Centre  
SPIN, F-42023, Saint–Etienne, France*

<sup>b</sup>*Dipartimento di Ingegneria Meccanica e Industriale, Università di Brescia, Via Branze  
38, 25123, Brescia, Italy*

---

## Abstract

We revisit the classical 2D problem of a gravity–driven liquid layer down an inclined plate (Kapitza, *Zh. Eksp. Teor. Fiz.*, vol. 18 (1), 1948, pp. 3–28), relaxing the usual assumption of homogeneous fluid. We set out to answer three major issues. When the fluid density is allowed to vary, (i) how does this feature structurally affect the formulation of a low–dimensional depth–averaged model? (ii) To what extent and (iii) by virtue of which physical mechanism does compressibility participate in the long–wave interfacial instability? To provide the relevant answers, (i) we first make use of a second–order asymptotic expansion in the shallowness parameter to develop a weakly–compressible boundary–layer system: starting from a two–equation momentum–integrated model, an additional barotropic equation of state is required for closure purposes. In this respect, (ii) a temporal linear stability analysis is performed: it is revealed that compressibility plays a destabilising role whose magnitude is enhanced at intermediately tilted configurations,

---

\*

*Email address: gianluca.lavalle@emse.fr (G. Lavallo)*

and the more the Reynolds number approaches the critical threshold in the incompressible limit. (iii) We finally interpret the ensuing dispersion relation under the convenient framework of two-wave hierarchy, initiated by Whitham (*Linear and Nonlinear Waves*, Wiley—Interscience, 1974): the primary instability gets promoted by the flow compressibility as it contributes to deceleration of dynamic waves most significantly in the low-inertia regime. Indeed, compressibility locally acts as a further boost to the inertia-based mechanism of Kapitza instability by amplifying flow-rate variations within the liquid film.

*Keywords:* falling liquid films, interfacial instability, low-dimensional models

*PACS:* 47.15.Cb, 47.20.Ma, 68.15.+e

*2000 MSC:* 76E17, 76E19, 76M45

---

## 1. Introduction

Liquid layers sliding down an incline are routinely encountered in nature and represent a cross-disciplinary and highly topical object of study. Starting with the pioneer studies of Kapitza father-son team (Kapitza, 1948; Kapitza and Kapitza, 1949), visual observations have revealed the development of a wide variety of intriguing patterns along the fluid interface, from simple sinusoidal perturbations to strongly non-periodic three-dimensional solitons (Chang, 1994; Alekseenko et al., 1994).

This issue is also of practical relevance in many biological and industrial processes (Craster and Matar, 2009). Cooling towers, distillation units, multi-phase heat exchangers, fluid-phase separators, jet-film devices, power

12 station condenser tubes, absorption columns, electrolytic cells, scrubbers for  
13 pollution abatement, injection systems for enhanced oil recovery, *etc.* all ben-  
14 efit from the strong effect of superficial waves on the underlying processes of  
15 heat and mass transfer. For instance, according to data reported by Frisk  
16 and Davis (1972), the heat transfer intensification by waves forming along  
17 a water film in presence of a co-current air flow attains more than 100 %  
18 with respect to the flat-film scenario. On the other hand, for some appli-  
19 cations such as coating operations, a uniform flow thickness is required and  
20 instabilities should be prevented (Weinstein and Ruschak, 2004).

21 So far, the majority of works on wavy falling films is performed assuming  
22 flow incompressibility, *i.e.* the density of a fluid element remains uniform and  
23 constant. However, in many fields of science and engineering, this assumption  
24 may constitute an oversimplification of the physical problem, possibly leading  
25 to inaccurate conclusions. One example is the transport of carbon dioxide in  
26 pipelines from the energy plants to the injection sites for CCUS applications.  
27 When supercritical carbon dioxide is employed as solvent or carrier, in fact,  
28 density turns out to be an essential parameter in determining the performance  
29 of such a technological process. In this context, avoiding the unbounded  
30 growth of superficial disturbances, which can result in the emergence of slugs  
31 or even structural damages (Lu et al., 2020), is necessary for the safety of  
32 the transport infrastructure.

33 Although the convective long-wave interfacial mode known as Kapitza  
34 instability (Kapitza, 1948) constitutes a long-standing knowledge in case of  
35 a tilted or vertical plate, a deep understanding of how density variations  
36 enter this paradigm is still lacking in the literature. Thus, the link between

37 the compressibility and the occurrence of the Kapitza instability needs to  
38 be clarified and has prompted us to address the following question: which  
39 are the main implications of density inhomogeneities on the onset of Kapitza  
40 instability in inclined falling liquid films?

41 Recently, the relevance of wavy film flows has led to a number of at-  
42 tempts to achieve models for the evolution of the film thickness and its mean  
43 velocity (or flow rate) and to find a compromise between the accuracy and  
44 the computational effort. In most cases, the flow description is not too far  
45 from its wavy-less configuration, designed as Nusselt state (Nusselt, 1916).  
46 This makes the long-wave asymptotic expansion a feasible approach, which  
47 forms the cornerstone of many models derived after the influential paper  
48 of Benney (1966), who developed an evolution equation for the film height  
49 by introducing a small-scale parameter. However, Benney's equation suffers  
50 of finite-time blow-up of the time-dependent solution. This problem was  
51 addressed by Shkadov (1967) assuming that streamwise variations are small  
52 as compared with those developing in the crosswise direction, and through  
53 pressure removal boundary layer equations (BLEs) ensue. These are then av-  
54 eraged over the fluid depth to capture the main physical features of the flow  
55 by means of integral variables. Nonetheless, Shkadov's system of equations  
56 fails in capturing the correct long-wave instability threshold. This issues  
57 was addressed by Ruyer-Quil and Manneville (1998, 2000), who introduced  
58 the weighted residual integral boundary-layer model (WRIBL) and assured  
59 model consistency by formulating a closure law for the wall shear stress.

60 In this paper, our purpose is to deal with a weakly inhomogeneous medium  
61 to investigate whether and how the action of a low compressibility enhances

62 or mitigates the onset of long-wave interfacial instability. We therefore start  
63 by applying Benney’s modelling strategy to a barotropic flow in a weakly-  
64 compressible scenario. We globally characterise it in terms of compressibility  
65 by means of the Mach number and formulate a coupled system of two evo-  
66 lution equations by making use of the depth-wise averaging method based  
67 on the classical long-wave expansion as in Lavalle et al. (2015, 2017), *i.e.* by  
68 integration of the momentum balance (momentum integral method or MIM).  
69 The resulting model is comprehensive of second-order viscous diffusion ef-  
70 fects, which allow us to achieve good agreement in the incompressible limit in  
71 terms of the cut-off wavenumber with the Orr-Sommerfeld solution (Kalli-  
72 adasis et al., 2013).

73 Our study focuses on the influence of compressibility on the development  
74 of linear surface waves on a liquid film falling down an inclined wall under  
75 a shear-free atmosphere (figure 1). For this, we consider the primary insta-  
76 bility of the weakly-compressible uniform base flow and solve the temporal  
77 stability problem based on the long-wave model equations. By doing this,  
78 we answer two additional questions: (i) how does compressibility affect the  
79 formulation of depth-integrated equations? (ii) Which physical mechanism  
80 does the compressibility trigger in the long-wave interfacial instability?

81 Behind the usual incompressible way of modelling falling liquid layers,  
82 it is assumed that the speed of sound, when compared to the convective  
83 velocity scale, is sufficiently high to be considered infinite. Therefore, (i)  
84 a unique velocity scale appears in the problem and (ii) the fluid density is  
85 uniform and constant. On the contrary, when a finite speed of sound is taken  
86 into account, the scenario significantly changes. (i) Convective transport and



87 pressure wave propagation occur at disproportional rates, thereby requiring a  
88 proper incorporation of an additional dimensionless group in the problem. In  
89 this regard, the Sarrau–Mach number can be used to express the magnitude  
90 of the fluid speed as compared to the sound speed within the same medium.  
91 In addition, (ii) the fact that density field is allowed to vary in space and  
92 time demands the introduction of an Equation of State (EoS) among the  
93 governing equations.

94 Unfortunately, very little attention, to the best of our knowledge, has  
95 been up to now devoted to the assessment of the impact of compressibility  
96 on the film long–wave instability. In fact, only a few works tried to tackle  
97 this issue.

98 An extension of long–wave models to weakly–compressible barotropic  
99 flows is first proposed by Richard (2021). Compressibility–related effects  
100 are captured by means of a dedicated Mach number, defined by means of  
101 the incompressible surface waves celerity, and, in the limit where the sound  
102 speed goes to infinity, the incompressible version of the model is correctly  
103 recovered. However, the system of four Favre–averaged equations derived  
104 by Richard (2021) is intended for simulation of coastal waves and the author  
105 frames his argumentation around the ultimate goal of correctly predicting  
106 tsunamis’ arrival time. Although the long–wave assumption still holds for a  
107 tidal wave in a deep ocean, the relevant spatial scales involved widely differs  
108 from the ones we are interested in. Moreover, in Richard (2021), the wave  
109 propagation is studied within an inviscid medium, neglecting viscous effects.

110 Such friction terms have also been neglected in the work of Bresch et al.  
111 (2020), who developed an augmented skew–symmetric system of depth–

112 integral equations with capillarity. Their work aims at ensuring the stability  
113 of numerical schemes in presence of large gradients of fluid height or fluid  
114 density.

115 In the context of flows within a narrow interstice formed between two  
116 surfaces, Almqvist et al. (2019) consider a class of iso-viscous fluids obeying  
117 a constitutive power-law density-pressure relationship. Lubrication theory,  
118 scaling and asymptotic analysis are extensively used in that work to show  
119 that the degree of compressibility for a thin film flow determines whether  
120 the terms governing inertia may or may not be neglected. Notwithstanding  
121 the rigorousness of their procedure, the study of a capillary flow is not at all  
122 comparable to a free-surface gravity-driven liquid film.

123 We conclude by recalling the fundamental results regarding the linear  
124 stability problem of a falling liquid film in a passive gas or shear-free at-  
125 mosphere, which is the configuration studied in this work. Benjamin (1957)  
126 and Yih (1963) solved the temporal linear stability problem formulated by Orr  
127 (1907) and Sommerfeld (1908) in the context of a gravity-driven incompress-  
128 ible film flow. In particular, they detected the long-wave instability threshold  
129 in terms of a critical Reynolds number  $Re_{cr} = 5/6 \cot \beta$ , where  $\beta$  identifies  
130 the inclination angle, being the Reynolds number based on the mean film  
131 flow velocity. Their analysis reveals that inertia destabilizes long waves and  
132 the related mechanism has been explained either through the shift between  
133 the vorticity perturbation and the perturbed interface (Kelly et al., 1989;  
134 Kalliadasis et al., 2013; Smith, 1990), or via the time lag at which flow rate  
135 adapts to its inertialess target value (Dietze, 2016). With the aim to inves-  
136 tigate the role of compressibility on the long-wave instability, we follow the

137 latter approach by considering the effect of compressibility on the inertialess  
138 flow rate, similarly to Lavalle et al. (2019), who applied the same methodol-  
139 ogy to explain the confinement-induced stabilisation of falling liquid films.  
140 Finally, we complement this analysis by studying the role of compressibility  
141 via the two-wave competition theory formulated by Whitham (Whitham,  
142 1974), and employed by Samanta et al. (2011) and Samanta (2014) for liquid  
143 films down a slippery inclined plane or for shear-imposed falling films.

144 Accordingly, the structure of our paper is as follows. Section § 2 contains  
145 the basic governing equations, the boundary conditions of the problem, and  
146 the definition of the principal dimensionless groups, together with the long-  
147 wave scaling. Then, the low-dimensional modelling is discussed in § 3, from  
148 the specification of the EoS to the derivation of the weakly-compressible  
149 integral model. This will serve in the second part of the manuscript, devoted  
150 to the linear temporal stability eigen-problem, whose compatibility yields the  
151 dispersion relation outlined in § 4. To follow, § 5 presents our main findings  
152 in terms of critical threshold and parametric study of celerity branches. The  
153 mechanism governing the influence of compressibility on the film stability is  
154 finally elucidated in § 6. Concluding remarks are summarised in § 7, while  
155 some details of the analysis that were not included in the main body of the  
156 text are given in the appendix for completeness.

## 157 **2. Flow configuration and theoretical formulation**

158 Herein we consider the two-dimensional compressible flow of a gravity-  
159 driven iso-viscous liquid film, falling along a tilted wall within a shear-  
160 free atmosphere, as sketched in figure 1. The liquid film is Newtonian.

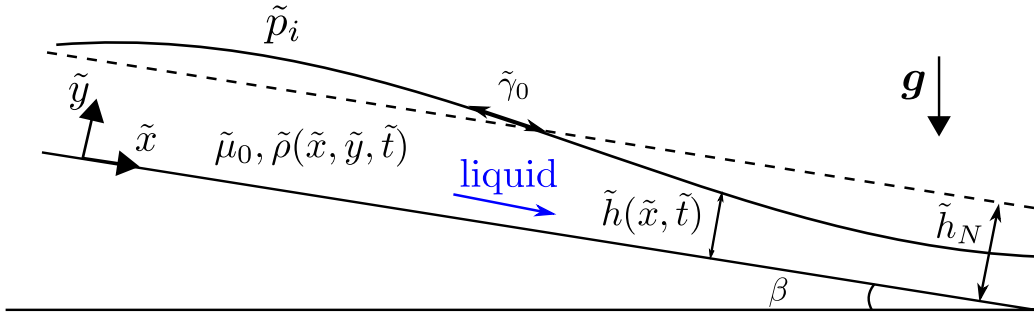


Figure 1: Schematic diagram of the 2D slightly compressible flow of a wavy gravity-driven liquid film with uniform and constant viscosity  $\tilde{\mu}_0$  and surface tension  $\tilde{\gamma}_0$ , exhibiting a non-uniform and variable density  $\tilde{\rho}(\tilde{x}, \tilde{y}, \tilde{t})$ . The coordinate system is defined by  $\langle \tilde{x}, \tilde{y} \rangle$ . The fluid layer, of variable thickness  $\tilde{h}(\tilde{x}, \tilde{t})$ , flows under the action of gravity  $\mathbf{g}$  along a plate having an inclination angle  $\beta$  with respect to the horizontal direction.  $\tilde{h}_N$  refers to Nusselt solution (Nusselt, 1916) and denotes the waveless film thickness. An interfacial constant and uniform normal pressure  $\tilde{p}_i$  is present.

161  $\beta \in ]0, \frac{\pi}{2}]$  refers to the angle of inclination formed between the wall and the  
 162 horizontal direction. The Cartesian coordinate axes  $\tilde{x}$  and  $\tilde{y}$  are placed along  
 163 the streamwise and crosswise flow directions, respectively, being the origin  
 164 of the spatial reference frame located at the wall;  $\tilde{t} \in \mathbb{R}_0^+$  specifies the time  
 165 coordinate. Assume that, with the exception of density  $\tilde{\rho} \in \mathbb{R}^+$ , the physi-  
 166 cal properties of the liquid, such as dynamic viscosity  $\tilde{\mu}_0 \in \mathbb{R}^+$  and surface  
 167 tension  $\tilde{\gamma}_0 \in \mathbb{R}^+$ , are uniform within the physical fluid domain  $\tilde{\Psi}$ , defined as

$$\tilde{\Psi}(\tilde{t}) = \left\{ (\tilde{x}, \tilde{y}) \in \tilde{\mathbb{R}}^2 \mid 0 \leq \tilde{y} \leq \tilde{h}(\tilde{x}, \tilde{t}) \right\}, \quad (1)$$

168 where  $\tilde{h}$  is a dimensional function tracing the spatial and temporal evolution  
 169 of the wavy film free surface.

170 *2.1. Governing equations*

171 At the continuum level, the dimensional form of the governing equations  
 172 of motion enforcing the conservation of mass and momentum for the com-  
 173 pressible flow of the Newtonian falling film reads:

$$\partial_{\tilde{t}} \tilde{\rho} + \tilde{\nabla} \cdot (\tilde{\rho} \tilde{\mathbf{v}}) = 0 \quad (2a)$$

$$\tilde{\rho} \left( \partial_{\tilde{t}} \tilde{\mathbf{v}} + (\tilde{\mathbf{v}} \cdot \tilde{\nabla}) \tilde{\mathbf{v}} \right) = -\tilde{\nabla} \tilde{p} + \tilde{\rho} \mathbf{g} + \tilde{\mu}_0 \left( \tilde{\nabla}^2 \tilde{\mathbf{v}} + \left( \frac{1}{3} + \vartheta \right) \tilde{\nabla} (\tilde{\nabla} \cdot \tilde{\mathbf{v}}) \right), \quad (2b)$$

174 where  $\tilde{\mathbf{v}} = (\tilde{u}, \tilde{v})$  and  $\tilde{p}$  denote, respectively, the film velocity vector and  
 175 the thermodynamic pressure, whereas  $\mathbf{g} = (g \sin \beta, -g \cos \beta)$  is the grav-  
 176 itational acceleration. The parameter labelled by  $\vartheta = \tilde{\zeta}_0 / \tilde{\mu}_0$  expresses the  
 177 ratio between the expansion viscosity  $\tilde{\zeta}_0 \in \mathbb{R}$  and the dynamic viscosity  
 178  $\tilde{\mu}_0$ . Although  $\vartheta$  is conventionally set to zero invoking Stokes' hypothesis  
 179 ( $\tilde{\zeta}_0 \equiv 0$ ) (Batchelor, 2000), we will not assume any particular value in or-  
 180 der to preserve the widest possible generality throughout the paper. As will  
 181 be demonstrated in § 3.2, this choice has no consequences in the ultimate  
 182 formulation of the reduced model (25).

183 The flow system is subject to the following boundary conditions. At the  
 184 rigid bottom  $\tilde{y} = 0$ , the no-slip and no-penetration conditions lead to

$$\tilde{\mathbf{v}}|_0 = \mathbf{0}. \quad (3)$$

185 At the free surface  $\tilde{y} = \tilde{h}(\tilde{x}, \tilde{t})$ , the balance of normal and tangential stress  
 186 components for the shear-free film yields the dynamic coupling conditions

$$\left[ \tilde{\mathbf{n}}^T \cdot \tilde{\mathbf{T}}^{(\tilde{\mathbf{n}})} \right] = \tilde{\gamma}_0 \tilde{\nabla} \cdot \tilde{\mathbf{n}} \quad (4a)$$

$$\left[ \tilde{\mathbf{t}}^T \cdot \tilde{\mathbf{T}}^{(\tilde{\mathbf{n}})} \right] = 0, \quad (4b)$$

187 where  $\tilde{\gamma}_0$  is the surface tension and  $\tilde{\mathbf{T}}^{(\tilde{\mathbf{n}})}$  is the fluid stress vector at the  
 188 interface, whose orientation is determined by

$$\tilde{\mathbf{n}} = \left\{ -\partial_{\tilde{x}}\tilde{h}, 1 \right\}^T / \sqrt{1 + \left(\partial_{\tilde{x}}\tilde{h}\right)^2} \quad (5a)$$

$$\tilde{\mathbf{t}} = \left\{ 1, \partial_{\tilde{x}}\tilde{h} \right\}^T / \sqrt{1 + \left(\partial_{\tilde{x}}\tilde{h}\right)^2} \quad (5b)$$

189 as normal and tangential unit column vector, respectively. Square brackets  
 190 are used in (4) to designate the jump in any quantity of interest across the in-  
 191 terface. Lastly, being the substantial derivative symbolised by  
 192  $D(\star)/D\tilde{t} = \partial_{\tilde{t}}(\star) + \tilde{\mathbf{v}} \cdot (\tilde{\nabla}\star)$ , an additional kinematic condition for the gas-  
 193 liquid interface is introduced as follows

$$\frac{D}{D\tilde{t}} \left( \tilde{y} - \tilde{h}(\tilde{x}, \tilde{t}) \right) = 0. \quad (6)$$

## 194 2.2. Scaling and dimensionless formulation

195 To make the problem dimensionless, we choose the value of the density at  
 196 the gas–fluid interface as the reference scale for density  $\tilde{\rho}_0$  in line with Richard  
 197 (2021). This scale is convenient since at  $\tilde{y} = \tilde{h}$  the hydrostatic contribution  
 198 on pressure and density fields is depth–independent. The Nusselt film thick-  
 199 ness  $\tilde{h}_N$  (Nusselt, 1916) is chosen as the relevant length scale (figure 1),  
 200 while we adopt the longitudinal characteristic speed as scale for the velocity  
 201  $\tilde{U}_N = \tilde{q}_N/\tilde{h}_N = \tilde{\rho}_0 g \sin \beta \tilde{h}_N^2 / 3 \tilde{\mu}_0$ , where  $\tilde{q}_N$  is the flow rate per unit of  
 202 channel length:

$$\tilde{q}_N = \int_0^{\tilde{h}_N} \tilde{u}_N(\tilde{y}) d\tilde{y}, \quad (7)$$

203 being  $\tilde{u}_N(\tilde{y})$  the well–known Nusselt parabolic velocity profile (Nusselt, 1916).

204 The average velocity  $\tilde{U}_N$  is indeed defined from the balance of the viscous  
 205 friction force,  $\propto \tilde{\mu}_0 \tilde{U}_N / \tilde{h}_N^2$ , and the streamwise gravity force,  $\propto \tilde{\rho}_0 g \sin \beta$ .

206 The time and pressure scales are chosen as  $\tilde{h}_N/\tilde{U}_N$  and  $\tilde{\rho}_0 \tilde{U}_N^2$ , respectively (Lavalle  
 207 et al., 2015).

208 As a customary practice in the study of the wavy film dynamics, we will  
 209 adopt a shallow water approximation. Denoting by  $\tilde{\mathcal{L}}$  a typical lengthwise  
 210 distance characterizing superficial corrugations, we define the following film  
 211 aspect ratio

$$\varepsilon = \frac{\tilde{h}_N}{\tilde{\mathcal{L}}} \ll 1, \quad (8)$$

212 as the scale parameter of the problem. Specifically,  $\varepsilon \sim \partial_{x,t}(\star)$  accounts for  
 213 the slowly-varying downstream modulations of the free surface with respect  
 214 to space and time.

215 Thus, the governing equations (2) are rewritten in dimensionless terms:

$$\partial_t \rho + \partial_x(\rho u) + \partial_y(\rho v) = 0 \quad (9a)$$

$$\begin{aligned} \rho \varepsilon (\partial_t u + u \partial_x u + v \partial_y u) = & -\varepsilon \partial_x p + \frac{\rho}{Fr} \sin \beta + \\ & + \frac{1}{Re} \left[ \partial_{yy} u + \varepsilon^2 \partial_{xx} u + \varepsilon^2 \left( \frac{1}{3} + \vartheta \right) \partial_x (\partial_x u + \partial_y v) \right] \end{aligned} \quad (9b)$$

$$\begin{aligned} \rho \varepsilon^2 (\partial_t v + u \partial_x v + v \partial_y v) = & -\partial_y p - \frac{\rho}{Fr} \cos \beta + \\ & + \frac{\varepsilon}{Re} \left[ \varepsilon^2 \partial_{xx} v + \partial_{yy} v + \left( \frac{1}{3} + \vartheta \right) \partial_y (\partial_x u + \partial_y v) \right], \end{aligned} \quad (9c)$$

216 being  $Re = \tilde{\rho}_0 \tilde{U}_N \tilde{h}_N / \tilde{\mu}_0$  and  $Fr = \tilde{U}_N^2 / g \tilde{h}_N$  the Reynolds number and the  
 217 Froude number, respectively, with  $(x, y, t) \in \mathbb{R} \times [0, h] \times [0, +\infty[$ .

218 The system (9) is coupled with the following set of dimensionless bound-

219 ary conditions:

$$u|_0 = v|_0 = 0 \quad (10a)$$

$$Re (1 + \varepsilon^2 \partial_x^2 h) (p|_h - p_i) + \varepsilon \left( \frac{2}{3} - \vartheta \right) (1 + \varepsilon^2 \partial_x^2 h) (\partial_x u|_h + \partial_y v|_h) + \quad (10b)$$

$$-2 \varepsilon (\partial_y v|_h + \varepsilon^2 \partial_x^2 h \partial_x u|_h) + 2 \varepsilon \partial_x h (\partial_y u|_h + \varepsilon^2 \partial_x v|_h) = -\frac{Re}{We} \frac{\varepsilon^2 \partial_{xx} h}{\sqrt{1 + \varepsilon^2 \partial_x^2 h}}$$

$$2 \varepsilon^2 \partial_x h (\partial_y v|_h - \partial_x u|_h) + (1 - \varepsilon^2 \partial_x^2 h) (\partial_y u|_h + \varepsilon^2 \partial_x v|_h) = 0 \quad (10c)$$

$$\partial_t h + u|_h \partial_x h = v|_h, \quad (10d)$$

220 where  $p_i$  is the dimensionless atmospheric pressure exerted at the film inter-  
 221 face and  $We = \tilde{\rho}_0 \tilde{h}_N \tilde{U}_N^2 / \tilde{\gamma}_0$  is the Weber number.

### 222 3. Low-dimensional modelling

223 Here, the free-surface flow problem is tackled adopting an asymptotic  
 224 approximation of the continuity and the Navier-Stokes equations based on  
 225 the film aspect ratio  $\varepsilon \ll 1$  introduced in § 2.2. A great simplification can  
 226 be accomplished by means of a boundary layer approach together with a  
 227 depth-averaging technique. Such a procedure leads to the determination of  
 228 a reduced coupled system of two equations, having the film thickness  $h(x, t)$   
 229 and the flow rate per unit of channel width  $q(x, t)$  as local dimensionless  
 230 unknowns. We propose a two-equation momentum-integral model (MIM)  
 231 that is accurate up to and including order  $O(\varepsilon^2)$  both in inertial and in  
 232 viscous diffusion terms. Based on this approximation, the problem expressed  
 233 by (9, 10) will be consistently simplified accounting for the higher magnitude  
 234 of surface tension,  $We = O(\varepsilon^2)$ , compared to inertia-related phenomena,  
 235  $Re \sim Fr = O(1)$ .



236 Following the classical Polhausen–von Kármán momentum–integral anal-  
 237 ysis, the  $y$ –momentum equation (9c) and related boundary condition (10b)  
 238 serve to eliminate the streamwise pressure gradient term  $\partial_x p$  in the  $x$ –momentum  
 239 equation (9b). Being this term of  $O(\varepsilon)$ , it is sufficient to retain (9c) and (10b)  
 240 up to  $O(\varepsilon)$ . Differently from the incompressible scenario, in this work, a sup-  
 241 plementary constitutive relation is required to describe completely the fluid  
 242 system due to the presence of a density term  $\rho = \tilde{\rho}/\tilde{\rho}_0 = O(1)$  as an addi-  
 243 tional unknown (Richard, 2021).

### 244 3.1. Barotropic equation of state

245 Since it is difficult to encounter large variations in density in gravity–  
 246 driven falling films, we make use of the following linearised Equation of State  
 247 (EoS)

$$\tilde{\rho}(\tilde{p}, \tilde{T}, \tilde{S}) = \tilde{\rho}|_{\tilde{h}} + \left(\frac{\partial \tilde{\rho}}{\partial \tilde{p}}\right)_{\tilde{T}, \tilde{S}} (\tilde{p} - \tilde{p}|_{\tilde{h}}) + \left(\frac{\partial \tilde{\rho}}{\partial \tilde{T}}\right)_{\tilde{p}, \tilde{S}} (\tilde{T} - \tilde{T}|_{\tilde{h}}) + \left(\frac{\partial \tilde{\rho}}{\partial \tilde{S}}\right)_{\tilde{p}, \tilde{T}} (\tilde{S} - \tilde{S}|_{\tilde{h}}), \quad (11)$$

248 in the form of a first–order truncated Taylor series expansion as in Batchelor  
 249 (2000); Colinet et al. (2001). The validity of (11) is intended to be restricted  
 250 to a neighborhood of the reference state, *i.e.*  $\tilde{\rho} - \tilde{\rho}|_{\tilde{h}} \ll 1$ . Specifically, besides  
 251 pressure  $\tilde{p}$ , the parameters that characterize such a functional dependence are  
 252 the fluid temperature  $\tilde{T}$  and its entropy  $\tilde{S}$  for a fixed vector of amounts of  
 253 constituents.

254 At the present stage, density–affecting thermal effects – which would  
 255 have required an energy equation coupling – will be ignored, so as to confine  
 256 our current inquiry to a two–equation MIM pattern. Moreover, although the  
 257 flow is not itself homentropic, the propagation of small–amplitude long–wave

258 perturbations is shown to be scarcely affected by acoustic attenuation and  
 259 dispersion phenomena (Van Dael, 1968; Kinsler et al., 2000). We postpone a  
 260 more rigorous proof of this statement to § 6.1, where we deal with the notion  
 261 of wave hierarchy.

262 Therefore, the EoS (11) is reduced to a *barotropic* formulation where  
 263 density variations with pressure support the propagation of sound waves:

$$\tilde{\rho}(\tilde{p}) = \tilde{\rho}_0 + \left( \frac{\partial \tilde{\rho}}{\partial \tilde{p}} \right)_{\tilde{s}} (\tilde{p} - \tilde{p}|_h). \quad (12)$$

264 Notably, one can refer to the thermodynamic definition of isentropic speed  
 265 of sound (Shapiro, 1953)

$$\tilde{a}_0 = \sqrt{\left( \frac{\partial \tilde{p}}{\partial \tilde{\rho}} \right)_{\tilde{s}}}, \quad (13)$$

266 whose magnitude  $\tilde{a}_0$  is supposed to be uniform and constant within  $\tilde{\Psi}$ , in  
 267 order to achieve the dimensionless version of (11), which ultimately reads

$$\rho(p) = 1 + Ma^2 (p - p|_h). \quad (14)$$

268 In (14) an overall Sarrau–Mach number

$$Ma = \frac{\tilde{U}_N}{\tilde{a}_0} \in \mathbb{R}^+, \quad (15)$$

269 expressing the magnitude of inertial forces with respect to elastic ones, has  
 270 been introduced as dimensionless group to capture the influence of compress-  
 271 ibility on the film flow. As it can be inferred from (14), the classical incom-  
 272 pressible limit is recovered as a limiting case when the acoustic propagation  
 273 is modelled as an instantaneous phenomenon, *i.e.*  $\tilde{a}_0 \rightarrow +\infty \iff Ma \rightarrow 0^+$ .

274 *3.1.1. Pressure distribution*

275 Replacement of (14) into the  $O(\varepsilon)$  estimate of (9c) leads to the following  
 276 first—order linear non—homogeneous Ordinary Differential Equation (ODE)  
 277 with respect to the crosswise coordinate  $y$  for the film pressure  $p(x, y, t)$ :

$$\partial_y p + \frac{\cos \beta}{Fr} Ma^2 p = \frac{\cos \beta}{Fr} (Ma^2 p|_h - 1) + \frac{\varepsilon}{Re} \partial_y \mathcal{W} + O(\varepsilon^2), \quad (16)$$

278 in which the function  $\mathcal{W}(u, v; \vartheta) = \partial_y v + \left(\frac{1}{3} + \vartheta\right) (\partial_x u + \partial_y v)$  implicitly de-  
 279 pends on  $y$  through the dimensionless velocity field. The solution of (16),  
 280 in which the dimensionless interfacial pressure  $p|_h$  has been evaluated using  
 281 the normal stress boundary condition (10b), is determined as summation of  
 282 the particular solution of (16) and the solution of the corresponding homoge-  
 283 neous ODE. The latter is obtained via the method of separation of variables,  
 284 whereas the former through the technique of variation of parameters (some-  
 285 times referred to as Duhamel’s principle). As a result, the proper solution  
 286 of (16) reads:

$$p(x, y, t; \vartheta) = p_i + \frac{\overbrace{\exp\left[\frac{\cos \beta}{Fr} Ma^2 (h - y)\right] - 1}^{\blacklozenge}}{Ma^2} - \frac{\varepsilon^2}{We} \partial_{xx} h + \frac{\varepsilon}{Re} \left( \mathcal{W} - (\partial_x u)|_h \right) + O(\underbrace{\varepsilon Ma^2}_{\clubsuit}), \quad (17)$$

287 being its full—form given in Appendix A. As expected, as the Mach number  
 288 approaches zero, (17) reduces to the pressure distribution obtained by Ruyer-  
 289 Quil and Manneville (1998) in the context of a perfectly incompressible free-  
 290 surface flow, by virtue of the exponential limit  $(e^{m \star} - 1)/\star \rightarrow m$  for vanish-  
 291 ing  $\star$  (with  $m \in \mathbb{R} \setminus \{0\}$ ), along with the incompressible continuity identity  
 292  $\partial_y v = -\partial_x u$ .

293 Based on the above considerations, the barotropic EoS (14) can be recast  
 294 as

$$\rho(x, y, t; \vartheta) = \underbrace{\exp\left[\frac{\cos\beta}{Fr}Ma^2(h-y)\right]}_{\blacklozenge} + O(\underbrace{\varepsilon Ma^2}_{\clubsuit}). \quad (18)$$

295 *3.1.2. Weak compressibility hypothesis*

296 Although the flow compressibility is taken into account in this model, thin  
 297 descending liquid films usually show a weakly compressible behaviour and,  
 298 therefore, the expression (18) can be simplified. To do so, the magnitude of  
 299 the Mach number can be estimated with respect to  $\varepsilon$  and, taking inspiration  
 300 from Richard (2021), we can write

$$Ma = M \varepsilon^\alpha, \quad (19)$$

301 where  $\alpha$  controls the compressibility behaviour and  $M = O(1) \in \mathbb{R}_0^+$ . As a  
 302 consequence, the accuracy of the model is retained only if  $\alpha \geq 1$  since the  
 303 residual term  $\clubsuit$  in (18) is of  $O(2\alpha + 1)$ . In our model, the Mach number  
 304 enters into the governing equations only through the barotropic EoS (14)  
 305 and, since  $Ma^2 = O(\varepsilon^{2\alpha})$ , the different orders in terms of integer power of  
 306 the Mach number can be classified as  $\alpha = \{1, 3/2, 2, 5/2, \dots\}$ .

307 An estimation of the order of magnitude of the exponential term  $\blacklozenge$   
 308 in (17, 18) within the low- $Ma$  limit requires one to take the Maclaurin se-  
 309 ries expansion  $e^\star = \sum_{n=0}^{\infty} (\star^n/n!)$ , that, together with the preliminary guess  
 310 about the order of magnitude of  $Fr = O(1)$ , yields to:

$$\underbrace{\exp\left[\frac{\cos\beta}{Fr}Ma^2(h-y)\right]}_{\blacklozenge} \approx 1 + \underbrace{\frac{\cos\beta}{Fr}Ma^2(h-y)}_{\blacklozenge_1} + \frac{1}{2} \underbrace{\left[\frac{\cos\beta}{Fr}Ma^2(h-y)\right]^2}_{\blacklozenge_2}, \quad (20)$$

311 implying that  $\blacklozenge_1 = O(\varepsilon^{2\alpha})$  and  $\blacklozenge_2 = O(\varepsilon^{4\alpha})$ . Depending on the value of  $\alpha$ ,  
 312 a twofold level of compressibility can be consequently addressed in view of  
 313 the prescribed  $O(\varepsilon^2)$  accuracy criterion:

$$\rho(x, y, t; \vartheta) = \begin{cases} 1 + O(\varepsilon^3), & \alpha \geq \frac{3}{2} \\ 1 + \frac{\cos\beta}{Fr} Ma^2 (h - y) + O(\varepsilon^3), & \alpha = 1. \end{cases} \quad (21)$$

314 Thus, when  $\alpha \geq 3/2$  the analysis is formally identical to the incompressible  
 315 scenario, since a relation of asymptotic equivalence holds between  $\tilde{\rho}(x, y, t)$   
 316 and  $\tilde{\rho}_0$ . In other words, the relation (19) provides a rule-of-thumb crite-  
 317 rion for the film flow to be considered as weakly-compressible in asymptotic  
 318 terms. For example, if we assume  $\varepsilon = 0.01$  as long-wave parameter (jointly  
 319 with a unitary-valued  $M$ ), we find the threshold for incompressibility as  
 320  $Ma \lesssim 0.001$ .

### 321 3.2. Boundary layer equations

322 In this this paper we focus on the weakly-compressible regime correspond-  
 323 ing to  $\alpha = 1$ . In this scenario, the derivative of the pressure distribution (17)  
 324 is computed using the expression (21) with  $\alpha = 1$ , leading to

$$\begin{aligned} \partial_x p(x, y, t; \vartheta) = & \frac{\cos\beta}{Fr} \partial_x h - \frac{\varepsilon^2}{We} \partial_{xxx} h + \\ & + \frac{\varepsilon}{Re} \left[ \partial_{xy} v + \left( \frac{1}{3} + \vartheta \right) \partial_x (\partial_x u + \partial_y v) - \partial_x ((\partial_x u)|_h) \right] + O(\varepsilon^2). \end{aligned} \quad (22)$$

325 As mentioned above, (22) is now substituted in lieu of  $\partial_x p$  in (9b), showing  
 326 that  $\vartheta$ -dependent contributions mutually cancel themselves out.

327 Then, the replacement of  $\rho$  and  $\partial_x p$  jointly permits obtaining the second-  
 328 order set of weakly compressible Boundary Layer Equations (BLEs), which

329 finally reads:

$$\partial_x u + \partial_y v + \frac{\cos \beta}{Fr} Ma^2 (\partial_t h + u \partial_x h - v) = 0 \quad (23a)$$

$$\begin{aligned} \varepsilon (\partial_t u + u \partial_x u + v \partial_y u) &= \frac{\partial_{yy} u}{Re} + \frac{\varepsilon^3}{We} \partial_{xxx} h - \varepsilon \frac{\cos \beta}{Fr} \partial_x h + \\ &+ \frac{\sin \beta}{Fr} \left( 1 + \frac{\cos \beta}{Fr} Ma^2 (h - y) \right) + \frac{\varepsilon^2}{Re} \left[ \partial_{xx} u - \partial_{xy} v + \partial_x ((\partial_x u)|_h) \right]. \end{aligned} \quad (23b)$$

330 By resorting to Leibniz's integral rule, BLEs (23) are integrated over the  
 331 depth  $\int_0^h (\star) dy$  to reduce the space dimensionality of the problem. The basic  
 332 idea behind this modelling strategy is the elimination of the cross-stream flow  
 333 dependency (Ruyer-Quil and Manneville, 2000).

334 Unfortunately, the resulting BLEs fail to be entirely expressed in terms of  
 335 the local film thickness  $h(x, t)$  and the local flow rate  $q(x, t) = \int_0^h u(y) dy$ .  
 336 Thus, closure laws are needed in (23b) for the following terms: the so-  
 337 called shape factor  $\int_0^h u^2 dy$ , the difference between interfacial and wall shear  
 338 stresses  $((\partial_y u)|_h - (\partial_y u)|_0)$ , and the antiderivative of other second-order terms  
 339 within square brackets ( $\propto \varepsilon^2/Re$ ). Moreover, since the compressibility intro-  
 340 duces a novel second-order contribution, related to the crosswise component  
 341 of velocity, *viz.*  $\int_0^h v dy$ , in (23a) an additional closure is required. Such  
 342 closures can be obtained via the explicit expression for the unknown velocity  
 343 field  $u(x, y, t)$ ,  $v(x, y, t)$ .

### 344 3.2.1. Long-wave approximation

345 In this work, we adopt a long wave approach following the classical Ben-  
 346 ney's closure technique (Benney, 1966; Gjevik, 1970; Lin, 1974; Chang, 1986).  
 347 Accordingly, each variable  $\mathcal{V} = \{u, v, p, \rho\}$  appearing in the primitive prob-  
 348 lem is decomposed as a formal power-series regular perturbation expansion,

349 having  $\varepsilon$  as basis:

$$\mathcal{V}^{(\varepsilon)} = \mathcal{V}^{(0)} + \varepsilon \mathcal{V}^{(1)} + \varepsilon^2 \mathcal{V}^{(2)} + \dots \quad (24)$$

350 The right-hand side of (24) is ideal for assessing the effect of a small per-  
351 turbation in  $\varepsilon$  about zero, provided that proper accuracy constraints are  
352 met (Simmonds and Mann Jr, 1998). Specifically, mathematical convergence  
353 of the infinite series (24) is not necessary (Jeffreys, 1926; Van Dyke and  
354 Rosenblat, 1975). On the other hand, it is required that – once truncated –  
355  $\mathcal{V}^{(\varepsilon)}$  rapidly approaches  $\mathcal{V}$  in the limit of vanishing  $\varepsilon$ . This is equivalent to  
356 enforce that the approximation error  $|\mathcal{V} - \mathcal{V}^{(\varepsilon)}|$  scales as the first neglected  
357 term of the series (24). By assuming this residue to be  $\sim \varepsilon^3$ , the  $O(\varepsilon^2)$   
358 truncation of the previous ansatz (24) can be then substituted in (9, 10, 14),  
359 allowing the corresponding equations to be broken up into different orders  
360 and sequentially solved. Specifically, the  $O(\varepsilon^0, \varepsilon^1)$  restrictions of the prob-  
361 lem coincide with their respective incompressible versions, due to the fact  
362 that  $Ma$ -related influence intervenes only at  $O(\varepsilon^2)$  when  $\alpha = 1$ , through the  
363 equality  $\rho^{(2)} = M^2 (p^{(0)} - p^{(0)}|_h)$  by (14). Also, the terms including the ex-  
364 pansion viscosity appear to be irrelevant, due to the fact that the  $O(\varepsilon^0, \varepsilon^1)$   
365 velocity fields are solenoidal. Hence, a comparison between the compressible  
366 second-order profiles and their incompressible analogues will be helpful to  
367 understand the impact of a varying density on flow-related quantities; this  
368 aspect will be discussed in § 6.2.

### 369 3.3. Depth-averaged model

370 Upon substitution, we now take advantage of the expressions for the  
371 asymptotic expansions determined beforehand. These are confined to Ap-

372 pendix B only for the sake of brevity.

373 In order to derive the depth–integral model, three steps need to be per-  
 374 formed: (i) replace higher–order time derivatives of  $h$  by virtue of a consis-  
 375 tent estimate of the kinematic boundary condition (10d), (ii) replace space  
 376 derivatives of  $q$  – except for the diffusive term  $\partial_{xx}q$  – by the corresponding  
 377 consistent asymptotic expansions, and (iii) add to the r.h.s. of (23b) the  
 378 higher–order residue  $+3(q^{(0)} + \varepsilon q^{(1)} + \varepsilon^2 q^{(2)} - q) / Re h^2 = O(\varepsilon^3)$ , so to pre-  
 379 clude algebraic cancellation of linear source terms – see (26) – as part of the  
 380 model quasi–linear reformulation (Lavalle et al., 2015). After these manip-  
 381 ulations, the following depth–averaged closed set of two evolution equations  
 382 is obtained:

$$\partial_t h + \partial_x q - \frac{\Lambda \cos \beta h^3 (\partial_x h)}{2 Fr} Ma^2 = 0 \quad (25a)$$

$$\begin{aligned} & \frac{h (\partial_x h) \cos \beta \varepsilon}{Fr} + \frac{3 h^4 (\partial_x h) \Lambda^2 \varepsilon}{5} + \varepsilon (\partial_t q) = \frac{h (\partial_{xxx} h) \varepsilon^3}{We} + \quad (25b) \\ & - \frac{4 Re h^5 (\partial_{xxxx} h) \Lambda \varepsilon^4}{21 We} - \frac{2 Re h^4 (\partial_x h) (\partial_{xxx} h) \Lambda \varepsilon^4}{3 We} + \\ & + \frac{2 Re h^4 (\partial_{xx} h)^2 \Lambda \varepsilon^4}{5 We} + \frac{4 Re h^3 (\partial_x h)^2 (\partial_{xx} h) \Lambda \varepsilon^4}{5 We} + \\ & + \frac{4 Re h^5 (\partial_{xx} h) \Lambda \cos \beta \varepsilon^2}{21 Fr} + \frac{16 Re h^4 (\partial_x h)^2 \Lambda \cos \beta \varepsilon^2}{15 Fr} + \\ & + \frac{3 Ma^2 h^2 \Lambda \cos \beta}{8 Fr Re} - \frac{8 Re h^8 (\partial_{xx} h) \Lambda^3 \varepsilon^2}{105} - \frac{23 Re h^7 (\partial_x h)^2 \Lambda^3 \varepsilon^2}{35} + \\ & + \frac{h^2 (\partial_{xx} h) \Lambda \varepsilon^2}{Re} + \frac{3 h (\partial_x h)^2 \Lambda \varepsilon^2}{Re} + \frac{2 (\partial_{xx} q) \varepsilon^2}{Re} + \frac{h \Lambda}{Re} - \frac{3 q}{Re h^2}, \end{aligned}$$

383 where the dimensionless number  $\Lambda$  is defined as  $Re/Fr \sin \beta$ . Here, by using  
 384 the definitions of  $\tilde{U}_N$ ,  $Re$  and  $Fr$ , we get that  $\Lambda = 3$ . In other contexts, this  
 385 parameter may assume different values, such as when a different character-  
 386 istic speed is used instead of Nusselt integral velocity  $\tilde{U}_N$ , in case of a fluid



387 exhibiting a non-Newtonian constitutive behaviour (Noble and Vila, 2013),  
388 or in presence of a variable or uneven interfacial pressure  $p_i$ ; it has been de-  
389 cided not to replace  $\Lambda$  by any numerical value (Richard et al., 2019) only to  
390 prevent loss of generality.

391 With reference to equation (25b), it is worth pointing out two additional  
392 facts. (i) Higher-order and non-linear capillary terms have been explicitly  
393 and fully retained, unlike what customarily developed (Ruyer-Quil and Man-  
394 neville, 1998; Richard et al., 2016, 2019). In fact, their contribution could be  
395 equally gathered on the l.h.s. within the canonical convective term propor-  
396 tional to  $\varepsilon \partial_x (q^2/h)$ , leading to an equivalent model in terms of consistency.  
397 (ii) Inertial terms have been maintained up to  $O(\varepsilon^2)$ , dissimilarly from the  
398 well-established practice of relying on a simplified model (Ruyer-Quil and  
399 Manneville, 2002). In fact, we are interested in comparing the whole second-  
400 order expansions with their incompressible analogues.

401 The derived shallow-water system (25) constitutes a second-order re-  
402 duced model describing the weakly-compressible free-surface flow of a wavy  
403 gravity-driven Newtonian falling film. In the scenario where the temperature  
404 field within the liquid film yields density variations, the EoS (12) should be  
405 modified accordingly to take into account density-affecting thermal effects.  
406 In addition, the model (25) should be coupled to an integral form of the  
407 energy equation to characterise the interplay between hydrodynamics, com-  
408 pressibility and heat transfer. For this, reduced models for non-isothermal  
409 (incompressible) falling films have been successful in solving the heat transfer  
410 across the liquid film (Trevelyan et al., 2007; Thompson et al., 2019; Cellier  
411 and Ruyer-Quil, 2020).

412 **4. Temporal linear stability**

413 A temporal stability analysis relies on the existence of a steady solution  
 414 about which perturbations are superimposed. Let  $\mathbf{Q}(x, t) = \{h(x, t), q(x, t)\}^T$   
 415 represent the column vector containing the two unknown integral variables  
 416 describing the film descent. Indeed, the weakly-compressible shallow-water  
 417 equations (25) possibly admit to be recast as

$$\partial_t \mathbf{Q} + \partial_x \mathcal{F}(\mathbf{Q}) = \mathcal{S}(\mathbf{Q}), \quad (26)$$

418 where  $\mathcal{F}$  is the associated flux vector whereas  $\mathcal{S}$  gathers source terms to-  
 419 gether (Noble and Vila, 2014).

420 *4.1. Normal mode analysis*

421 The linear stability problem of the low-dimensional weakly-compressible  
 422 model (25) is approached through normal mode decomposition, according to  
 423 which a harmonic infinitesimal disturbance  $\mathbf{Q}_p$ , having  $\|\hat{\mathbf{Q}}\| \ll 1$  as ampli-  
 424 tude, is added to the Nusselt base state. The latter is explained in terms  
 425 of the dimensionless uniform parallel solution  $\mathbf{Q}_0 = \{h_0, q_0\}^T$ , in which  
 426  $h_0 = \tilde{h}_0/\tilde{h}_N \equiv 1$  by definition, whereas the novel expression for the com-  
 427 pressible primary discharge  $q_0$  will be disclosed as part of the linearisation  
 428 process. Accordingly, it is written

$$\mathbf{Q}(x, t) = \mathbf{Q}_0 + \mathbf{Q}_p(x, t) \quad (27a)$$

$$\mathbf{Q}_p(x, t) = \hat{\mathbf{Q}} \exp[i k (x - c t)], \quad (27b)$$

429 where it remains understood that  $k = 2\pi \tilde{h}_N/\tilde{\mathcal{L}} \in \mathbb{R}^+$  and  $c = c_r + i c_i \in \mathbb{C}$   
 430 are, respectively, the dimensionless real wave-number and the complex wave

431 celerity of the propagating sine-type pulse. In particular,  $c_r$  accounts for its  
 432 phase velocity, whereas  $k c_i$  determines its degree of amplification or damping,  
 433 depending on its sign: with reference to (27b), instability of the mean flow  
 434 evidently sets in on the condition that  $k c_i > 0$ .

#### 435 4.1.1. Base flow calculation

436 Quasi-linear conservation form (26) actually stipulates a formal relation  
 437 between differential operators (Meliga et al., 2010) in such a way that

$$\mathcal{S}(\mathbf{Q}_0) = 0 \quad (28)$$

438 restores the equilibrium condition constraining the dimensionless compress-  
 439 ible base flow rate  $q_0(Re, \beta, Ma)$  to the dimensionless waveless thickness  $h_0$ .  
 440 Solving (28) we find:

$$q_0 = \frac{\Lambda h_0^3}{3} \left( 1 + \overbrace{\frac{3}{8} \frac{Ma^2 \Lambda \cot \beta h_0}{Re}}^{\Delta q_{0, \text{rel}}^{(2)}} \right), \quad (29)$$

441 which explicitly shows that compressibility entails a relative increase in the  
 442 equilibrium flow rate  $q_0$ , according to the over-bracketed second-order contri-  
 443 bution denoted as  $\Delta q_{0, \text{rel}}^{(2)}$ , with respect to its incompressible limit  
 444  $q_0^{Ma \rightarrow 0^+} = \Lambda h_0^3/3$ . Expression (29) likewise coincides with the stationary  
 445 waveless solution associated to system (23) in the case of unidirectional flow.  
 446 Compressible effects are kept at the base flow level  $\mathbf{Q}_0$ , on which linear distur-  
 447 bances  $\mathbf{Q}_p$  develop, by means of a small additive contribution to the incom-  
 448 pressible ground-state flow rate  $q_0^{Ma \rightarrow 0^+}$ . Such a correction ( $q_0^{Ma \rightarrow 0^+} \Delta q_{0, \text{rel}}^{(2)}$ )  
 449 appears to be of  $O(\varepsilon^2)$  since, choosing  $\alpha = 1$ , we assumed  $Ma$  to be of order  
 450  $O(\varepsilon)$ .

451 *4.1.2. Model dispersion relation*

452 Dropping higher-order perturbations and plugging (27) into (25) yields  
 453 the following matrix-form differential system:

$$\begin{aligned} \partial_t \mathbf{Q}_p + \begin{bmatrix} a_{11} & 1 \\ a_{21} & 0 \end{bmatrix} \partial_x \mathbf{Q}_p = \begin{bmatrix} 0 & 0 \\ b_{21} & b_{22} \end{bmatrix} \mathbf{Q}_p + \\ + \begin{bmatrix} 0 & 0 \\ c_{21} & c_{22} \end{bmatrix} \partial_{xx} \mathbf{Q}_p + \begin{bmatrix} 0 & 0 \\ s_{21} & 0 \end{bmatrix} \partial_{xxx} \mathbf{Q}_p + \begin{bmatrix} 0 & 0 \\ d_{21} & 0 \end{bmatrix} \partial_{xxxx} \mathbf{Q}_p, \end{aligned} \quad (30)$$

454 where

$$a_{11} = -\frac{Ma^2 h_0^3 \Lambda^2 \cot \beta}{2 Re} \quad b_{21} = \frac{3 \Lambda}{Re} + \frac{3 Ma^2 h_0 \Lambda^2 \cot \beta}{2 Re^2} \quad (31a)$$

$$a_{21} = \frac{3}{5} h_0^4 \Lambda^2 + \frac{h_0 \Lambda \cot \beta}{Re} \quad b_{22} = -\frac{3}{Re h_0^2} \quad c_{22} = \frac{2}{Re} \quad s_{21} = \frac{h_0}{We} \quad (31b)$$

$$c_{21} = \frac{4}{21} h_0^5 \Lambda^2 \cot \beta - \frac{8}{105} Re h_0^8 \Lambda^3 + \frac{h_0^2 \Lambda}{Re} \quad d_{21} = -\frac{4}{21} \frac{Re h_0^5 \Lambda}{We}. \quad (31c)$$

455 Expressions (31b – 31c) do not incorporate the Mach number, thus  $\varepsilon$  has  
 456 been legitimately replaced there by a unitary value (Richard et al., 2019).  
 457 Such assignment is based on the fact that pertinent orders of magnitude have  
 458 been already accounted for in the integral model (25).

459 Equation (30) accounts for the normal mode evolution (27b) under the  
 460 form of a generalised algebraic eigenvalue problem for  $c$  and  $\hat{\mathbf{Q}}$ , having  
 461  $\langle k; Re, \beta, We, Ma \rangle$  as independent set of relevant parameters. Seeking  
 462 a non-trivial solution, one has to impose that the matrix associated to the  
 463 linearised system is degenerate. This leads to a quadratic polynomial dis-  
 464 persion relation over the complex field in the phase speed  $c$  with complex  
 465  $k$ -dependent coefficients, written as

$$\begin{aligned}
& -k c^2 + [a_{11} k + i (b_{22} - k^2 c_{22})] c + \\
& + k^3 s_{21} + k a_{21} + i [d_{21} k^4 + (a_{11} c_{22} - c_{21}) k^2 + (b_{21} - a_{11} b_{22})] = 0. \quad (32)
\end{aligned}$$

466 *4.2. Celerity long-wave expansion*

467 Following Yih (1963), we consider the temporal stability problem in terms  
468 of an asymptotic expansion of the wave celerity  $c(k)$  into successive powers  
469 of the wavenumber  $k$ :

$$c = c^{(0)} + k c^{(1)} + k^2 c^{(2)} + k^3 c^{(3)} + \dots, \quad (33)$$

470 within the limit provided by the long-wave approximation ( $k \ll 1$ ) assumed  
471 in this work. In analogy with the closure algorithm illustrated in § 3.2.1,  
472 the expansion (33) is substituted into the dispersion relation (32). Ensuring  
473 that each order in  $k$  satisfies (32), we get a cascade of equations from which  
474 the higher-order celerities  $c^{(n)}(k)$  ( $n = 0, 1, 2, \dots$ ) are obtained. Although  
475 evolution equations (25) are consistent up to  $O(\varepsilon^2)$ , we intentionally take  
476 the expansion (33) for the celerity  $c(k)$  up to its successive order in terms of  
477  $k$ , that is until  $O(k^3)$ . In this way, we can test the accuracy of the present  
478 model (25) in its incompressible limit  $Ma \rightarrow 0^+$ , by setting the benchmark  
479 against the Orr–Sommerfeld stability problem (Orr, 1907; Sommerfeld, 1908)  
480 at the corresponding order. Such a comparative approach constitutes a well-  
481 trodden path among the falling-film community (Ruyer-Quil and Manneville,  
482 1998; Samanta et al., 2011; Samanta, 2014; Richard et al., 2016). Specifically,

483 we obtain:

$$c^{(0)} = 3 \quad (34a)$$

$$c^{(1)} = 3i \left( \frac{2}{5} Re - \frac{1}{3} \cot \beta + \Gamma_2^{(1)} Ma^2 \cot \beta \right) \quad (34b)$$

$$c^{(2)} = 3 \left( -1 + \frac{10}{21} Re \cot \beta - \frac{4}{7} Re^2 + \Gamma_2^{(2)} Ma^2 \cot \beta + \Gamma_4^{(2)} Ma^4 \cot^2 \beta \right) \quad (34c)$$

$$c^{(3)} = 3i \left( -\frac{1}{9} Re \cot^2 \beta + \frac{128}{105} Re^2 \cot \beta + \frac{2}{9} \cot \beta - \frac{Re}{9We} - \frac{228}{175} Re^3 + \right. \quad (34d)$$

$$\left. -\frac{34}{15} Re + \Gamma_2^{(3)} Ma^2 \cot \beta + \Gamma_4^{(3)} Ma^4 \cot^2 \beta + \Gamma_6^{(3)} Ma^6 \cot^3 \beta \right),$$

484 in which we use the equality  $\Lambda = 3$  and the identity  $h_0 \equiv 1$ . Those expres-  
 485 sions for the wave celerities have been written to highlight the effect of the  
 486 compressibility. In fact, the expansions (34) are impacted by compressibility  
 487 from  $n = 1$  onwards ( $n = 1, 2, \dots$ ) through additive contributions that take  
 488 the form  $\Gamma_{2j}^{(n)} Ma^{2j} \cot^j \beta$ , with  $1 \leq j \leq n$ . These are found to be:

$$\Gamma_2^{(1)} = \frac{3}{2} \quad \Gamma_2^{(2)} = \frac{1}{2} \cot \beta - \frac{18}{5} Re - \frac{1}{Re} \quad (35a)$$

$$\Gamma_4^{(2)} = -\frac{9}{4} \quad \Gamma_2^{(3)} = \frac{19}{7} Re \cot \beta - \frac{324}{35} Re^2 - \frac{9}{2} \quad (35b)$$

$$\Gamma_4^{(3)} = \frac{3}{4} \cot \beta - \frac{243}{20} Re - \frac{3}{2Re} \quad \Gamma_6^{(3)} = -\frac{27}{8}. \quad (35c)$$

489 In accordance with the adopted standard of accuracy, the current model  
 490 is consistent with the asymptotic expansions of solutions to Orr–Sommerfeld  
 491 boundary–value problem, reported in Ruyer-Quil and Manneville (1998), in  
 492 the limit of  $Ma \rightarrow 0^+$ : (25) is able to correctly recover  $c^{(0)}$ ,  $c^{(1)}|_{Ma \rightarrow 0^+}$  and  
 493  $c^{(2)}|_{Ma \rightarrow 0^+}$ , but it manifests disagreements on successive orders. For more  
 494 in–depth reflection on such validation the reader is referred to Appendix  
 495 C, being the primary focus of sections §§ 4, 5 upon the influence of a weak  
 496 compressibility on the linear stability.

## 497 5. Results and discussion

498 In this section we examine the relations (34) in the light of the well-known  
499 results from Kapitza (1948) and Benjamin (1957). The  $O(k^0)$  celerity (34a)  
500 immediately captures the classical phase speed of free-surface waves, which  
501 travel three times faster than the averaged flat film, regardless of its com-  
502 pressible behavior. Due to the nature of (14) as EoS, the compressibility  
503 terms controlled by the Mach number affect only even powers  $Ma^{2j}$  through-  
504 out  $O(k^n)$  expansions (34b – 34d), for  $1 \leq j \leq n$ .

505 Secondly, as evidenced by the relations (34) and (31a), a vertical liquid  
506 film is not affected by the compressibility since  $\cot(\frac{\pi}{2}) = 0$  in (25). On  
507 the other hand, when the plate is horizontal,  $\beta = 0$  and no gravity-driven  
508 drainage is possible.

### 509 5.1. Impact of compressibility on the wave celerity

510 Differently from the incompressible Navier–Stokes equations, whose tem-  
511 poral stability analysis is pursued through numerical solution of the Orr–  
512 Sommerfeld fourth-order differential problem in the cross-stream coordinate,  
513 in this case the dispersion relation (32) is a quadratic polynomial equation  
514 in  $c(k)$ , which is easily solvable numerically.

515 Initially, we consider a falling liquid film whose incompressible flow is  
516 marginally stable. This case will be shown to be the most favourable to  
517 discern compressibility-related effects on the film flow stability within the  
518 investigated weakly-compressible regime. The plate is angled at  $\beta = 4.6^\circ$ .  
519 As an aside, this choice enables us to compare the wave celerity and growth  
520 rate (see Appendix C) between the results presented here within the incom-

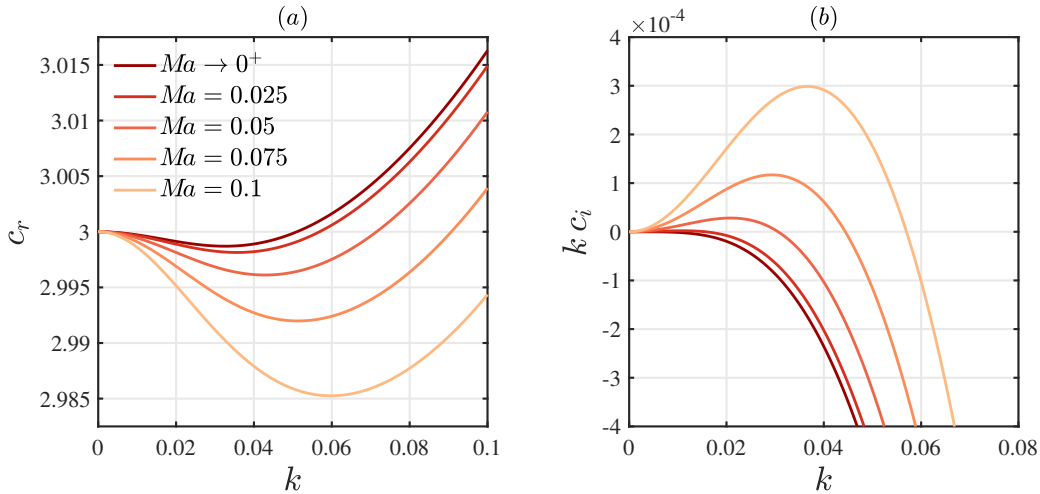


Figure 2: Impact of compressibility on the graphical representation of solutions to the dispersion relation (32) for the second-order integral model (25), in terms of (a) phase speed  $c_r$  and (b) growth rate  $k c_i$  as a function of the dimensionless wavenumber  $k$ , for different small values of the Mach number  $Ma$ , displayed in the legend. The axes are dimensionless. The data used are taken from Brevdo et al. (1999) and correspond to the following set of values:  $g = 9.81 \text{ m s}^{-2}$ ,  $\beta = 4.6^\circ$ ,  $Re = 5/6 \cot \beta = 10.357$ ,  $\tilde{\rho}_0 = 1130 \text{ kg m}^{-3}$ ,  $\tilde{\mu}_0 = 5.673 \cdot 10^{-3} \text{ Pa s}$ ,  $\tilde{\gamma}_0 = 69.0 \cdot 10^{-3} \text{ N m}^{-1}$ . Comparison with Brevdo et al. (1999) is shown in Appendix C for the incompressible scenario.

521 pressible limit  $Ma \rightarrow 0^+$  (dark red line in figure 2) and those determined  
522 by Brevdo et al. (1999) for a perfectly incompressible falling film in a passive  
523 atmosphere. The effects of compressibility on the hydraulic branch solv-  
524 ing (32) both in its real and imaginary parts are displayed in figure 2a, b  
525 respectively, for sufficiently small values of the Mach number  $Ma = O(\varepsilon)$ .  
526 Specifically, the evolution of the phase speed  $c_r(k)$  bends downwards as the  
527 Mach number increases. Nonetheless, the same long-wave limit  $c^{(0)}$  is re-  
528 covered, as established by (34a). The delaying effect of compressibility on  
529 the phase velocity of linear waves (Richard et al., 2019) finds confirmation in



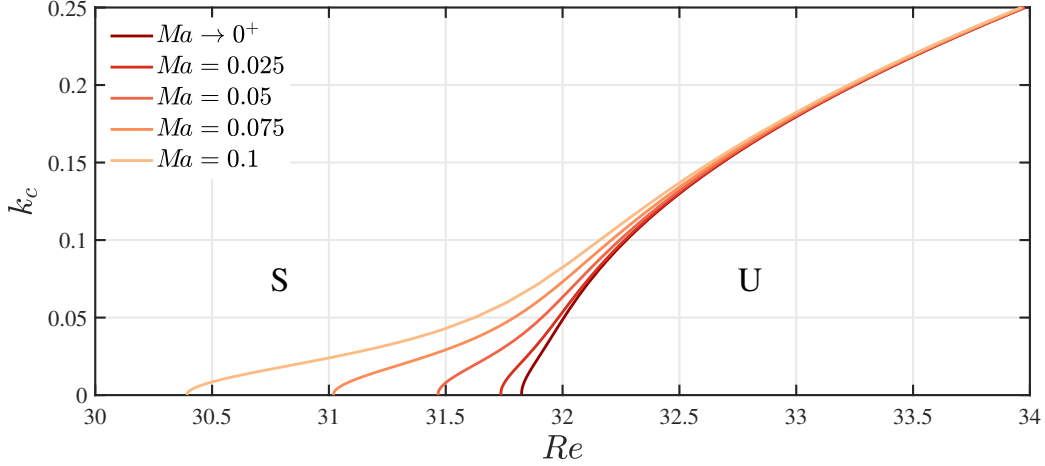


Figure 3: Impact of compressibility on the neutral stability diagram displaying the dimensionless cut-off wavenumber  $k_c$  as a function of the Reynolds number  $Re$ , for different small values of the Mach number  $Ma$ , shown in the legend. Parameter values:  $g = 9.81 \text{ m s}^{-2}$ ,  $\beta = 1.5^\circ$ . Fluid physical properties – related to a falling film consisting of a water–glycerin mixture – are taken from Liu and Gollub (1994):  $\tilde{\rho}_0 = 1070 \text{ kg m}^{-3}$ ,  $\tilde{\mu}_0 = 6.72 \cdot 10^{-3} \text{ Pa s}$ ,  $\tilde{\gamma}_0 = 67.0 \cdot 10^{-3} \text{ N m}^{-1}$ . The *stable* and *unstable* domain in the  $(Ma, Re)$  plane corresponds to areas labelled, respectively, “S” and “U”.

530 our study. The growth rate  $k c_i(k)$  shown in figure 2b deviates upwards and  
 531 towards increasing cut-off wavenumber  $k_c$  for growing  $Ma$ . Thus, compress-  
 532 ibility plays a destabilising role on linear free-surface waves.

533 Even more distinctly, we observe this feature in figure 3, which shows the  
 534 curve of marginal stability obtained for different values of the Mach number  
 535 in the  $(Re, k_c)$  plane for  $\beta = 1.5^\circ$ . Above the marginal stability curve, per-  
 536 turbations of wavenumber  $k$  decay in time, whereas they are amplified below.  
 537 Here, the unstable region systematically undergoes a non-linear enlargement  
 538 up to a smaller critical Reynolds number  $Re_{cr}$  due to the compressibility.

539 In order to quantify this shift into the stability threshold, we can examine

540 the first-order expansion of the wave celerity  $c^{(1)}$ , which for  $Ma \ll 1$  yields  
 541 the following relation

$$Re_{cr} = \frac{5}{6} \left( 1 - \frac{9}{2} Ma^2 \right) \cot \beta, \quad (36)$$

542 obtained by making  $Re$  explicit from (34b) when the neutral stability condi-  
 543 tion  $k c_i(k_c) = 0 \iff c^{(1)}|_{Re_{cr}} = 0$  is imposed. In the limit of null Mach num-  
 544 ber, equation (36) reduces to the result of Benjamin (1957) and Yih (1963),  
 545 *i.e.*,  $Re_{cr}^{Ma \rightarrow 0^+} = 5/6 \cot \beta$ . Conversely, we observe that for  $Ma = O(\varepsilon) > 0$   
 546 the compressibility lowers the critical Reynolds number  $Re_{cr}$  by a factor equal  
 547 to

$$\frac{Re_{cr}(Ma)}{Re_{cr}^{Ma \rightarrow 0^+}} = 1 - \frac{9}{2} Ma^2 < 1, \quad (37)$$

548 anticipating the flow primary instability. This effect tends to asymptotically  
 549 vanish in highly inertial regimes, within which compressible curves visibly be-  
 550 come rapidly convergent towards the incompressible marginal stability plot  
 551 (right-most line in figure 3). This finding is consistent as both the two com-  
 552 pressible coefficients (31a) of the eigen-problem (30) are inversely propor-  
 553 tional to the Reynolds number or its square power. Interestingly, we remark  
 554 that the ratio expressed by (37) is independent of the plate inclination  $\beta$ .

## 555 5.2. Parametric analysis

556 Aiming at understanding the basic effects of compressibility on the film  
 557 destabilisation, we investigate how the growth rate of disturbances  $k c_i$  evolves  
 558 as the parameter space, namely  $\langle Re, \beta, We, Ma \rangle$ , is explored. This will en-  
 559 able us to understand the fundamental physical mechanism through which  
 560 compressibility acts, which we examine more in depth in § 6.

561 We start by providing a variety of numerical solutions to the linear sta-  
562 bility problem (30) within the plane  $(k, k c_i)$ , for different values of the  
563 Reynolds number  $Re$  and angle of inclination  $\beta$ . Equations (34) suggest  
564 that a polynomial-type dependence is established by the novel  $Ma^{2j}$ -related  
565 contributions, namely  $\Gamma_{2j}^{(n)} \cot^j \beta$ . Unfortunately, the coefficients  $\Gamma_{2j}^{(n)}$  display  
566 a fairly cumbersome functional dependence on  $\cot \beta$  (as well as on  $Re$ ) –  
567 apart from when  $j = n$ . For this reason, notwithstanding that the compress-  
568 ibility has no impact on a vertical falling film, it is not possible to determine  
569 *a priori* whether its effects varies with the inclination. Therefore, we will  
570 extensively cover the full range of variability in  $\beta$ , starting by focusing on  
571 mildly tilted configurations.

572 In figure 4 we initially consider four cases, denoted with letters  $(a-d)$ ,  
573 which differ from each other in terms of slope. To draw an appropriate  
574 comparison among these scenarios between each compressible curve ( $Ma =$   
575  $0.1$  – dashed lines) and its incompressible counterpart (solid lines), the so-  
576 defined Reynolds critical ratio RCR

$$\text{RCR} \stackrel{\text{def}}{=} \frac{Re}{Re_{cr}^{Ma \rightarrow 0^+}} \quad (38)$$

577 is introduced as an inertia-based parameter. Four growing values of RCR  
578 are considered in each of the panels of figure 4, starting from a value which  
579 is numerically less than unity – which indicates a stable situation for a per-  
580 fectly incompressible falling film flow – before moving to values of  $Re$  which  
581 progressively exceed the critical incompressible threshold.

582 As expected, the augmentation of RCR is associated with the extension  
583 of the instability region  $c_i(k) > 0$ . When we switch from each incompressible  
584 plot to its compressible analogue, the rightwards shift of the cut-off wavenum-

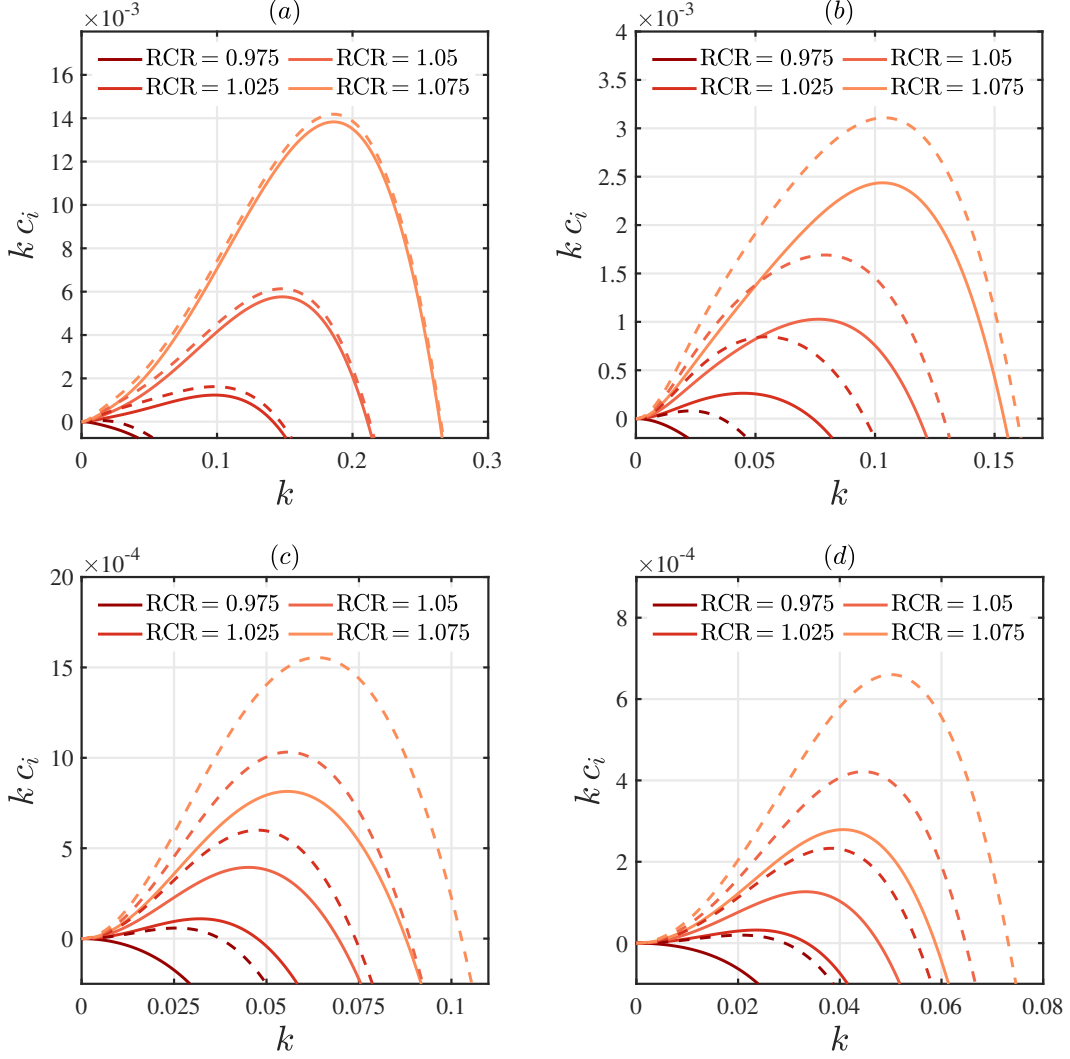


Figure 4: Effect of the Reynolds critical ratio RCR (38) (shown in the legend) on the graphical representation of the solution to the dispersion relation (32) for the derived weakly-compressible second-order model (25), in terms of the dimensionless imaginary growth rate  $k c_i$  as a function of the dimensionless wavenumber  $k$ , for flow configurations which differ from each other in the value of the inclination angle  $\beta$ : (a)  $\beta = 1.5^\circ$ , (b)  $\beta = 3.0^\circ$ , (c)  $\beta = 6.0^\circ$ , (d)  $\beta = 12.0^\circ$ . The axes are dimensionless. Solid lines:  $Ma \rightarrow 0^+$  (incompressible case), dashed lines:  $Ma = 0.1$ . Apart from the tilt angle  $\beta$ , other parameter values and fluid physical properties employed here are those of figure 3.

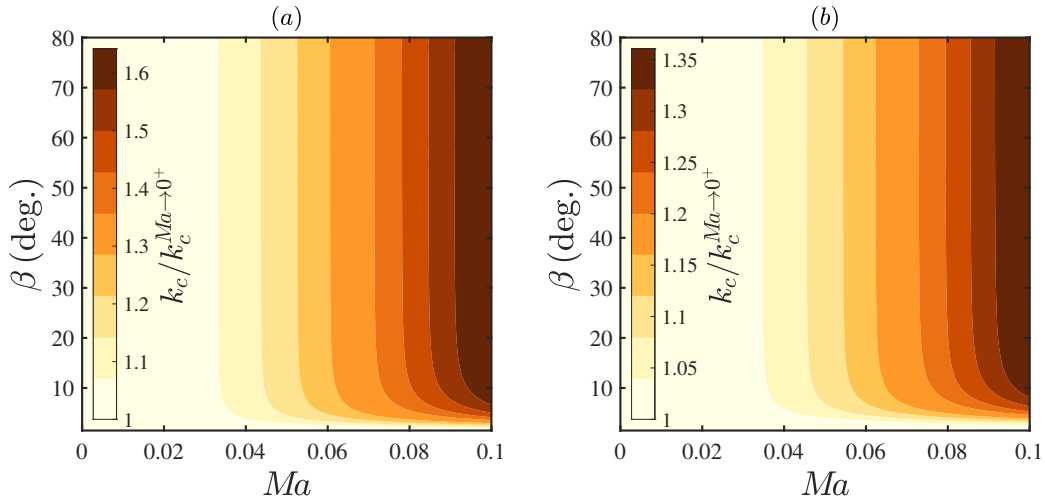


Figure 5: Effect of the Mach number  $Ma = O(\varepsilon)$  and of the angle of inclination  $\beta$  on the stability of a falling water–glycerin film in terms of deviation of the cut–off wavenumber  $k_c$  from its incompressible limit  $k_c^{Ma \rightarrow 0^+}$  with reference to the temporal growth rate of linear disturbances  $k c_i(k)$ , for two different fixed values of the Reynolds critical ratio (38), corresponding to (a)  $\text{RCR} = 1.025$  and (b)  $\text{RCR} = 1.05$ . In overall terms, darker regions correspond to a greater destabilisation. The set of parameter values and fluid physical properties is the same specified for figure 3.

585 ber  $k_c$  is reduced as the RCR is raised. This is in accordance with what  
 586 previously shown in figure 3. As the incline of the plate becomes steeper,  
 587 provided that moderately low–angle configurations are explored, the com-  
 588 pressibility plays an increasingly important effect in relative terms in terms  
 589 of a rightward shift of the dispersion curves.

590 In order to better appreciate this phenomenon, we represent in figure 5  
 591 the contours of the cut–off wavenumber related to its incompressible limit  
 592  $k_c/k_c^{Ma \rightarrow 0^+}$  as a function of the Mach number  $Ma$  and of the inclination  
 593 angle  $\beta$  for two different values of Reynolds critical ratio RCR beyond the

594 stability threshold, corresponding to (a)  $\text{RCR} = 1.025$  and (b)  $\text{RCR} = 1.05$ ,  
595 respectively. In both scenarios we identify two distinct regions of the  $(Ma, \beta)$   
596 plane: (i) a low-angle region ( $1.5^\circ \lesssim \beta \lesssim 12^\circ$ ) where compressibility-induced  
597 destabilisation is not fully-developed in terms of rightward shift of the cut-  
598 off wavenumber and (ii) a region that covers moderately to highly tilted  
599 configurations ( $12^\circ \lesssim \beta \lesssim 80^\circ$ ), where the same effects are independent of  
600 the value of inclination angle  $\beta$ . From a graphical point of view, the isolines  
601 rapidly tend to become vertical, indicating a fast saturation of  $k_c/k_c^{Ma \rightarrow 0^+}$   
602 with respect to slope.

603 Within area (ii), at  $Ma = 0.1$  – the highest level of weak compressibility  
604 investigated – the cut-off wavenumber is increased by up to roughly 60%  
605 when  $\text{RCR} = 1.025$  and 35% when  $\text{RCR} = 1.05$  in comparison with the in-  
606 compressible case. As it will soon become clear, there exists a third upper  
607 region (iii) – for  $80^\circ \lesssim \beta \leq 90^\circ$  – which is difficult to explore by employ-  
608 ing the parameter  $\text{RCR}$  since, there, a vertically falling film flow is always  
609 unstable to linear perturbations (Benjamin, 1957; Yih, 1963).

610 A similar behavior is shown by the most unstable wavenumber and the  
611 maximum growth rate of linear disturbances related to their incompressible  
612 limit, *viz.*  $k_{\max}/k_{\max}^{Ma \rightarrow 0^+}$  and  $\omega_{i, \max}/\omega_{i, \max}^{Ma \rightarrow 0^+}$  respectively, which are displayed  
613 in figure 6*a, b* as a function of the Mach number  $Ma$  and the inclination  
614 angle  $\beta$  in the case of a Reynolds critical ratio equal to  $\text{RCR} = 1.05$ . The  
615 results are shown up to  $\beta = 40^\circ$ , as the isocontour does not change in the  
616 region  $40^\circ < \beta < 80^\circ$ , as discussed before. The most unstable wavenumber  
617 increases up to 35% compared with its incompressible analogue. Also, the  
618 compressibility induces a similar increase of  $k_c/k_c^{Ma \rightarrow 0^+}$  and  $k_{\max}/k_{\max}^{Ma \rightarrow 0^+}$ ,

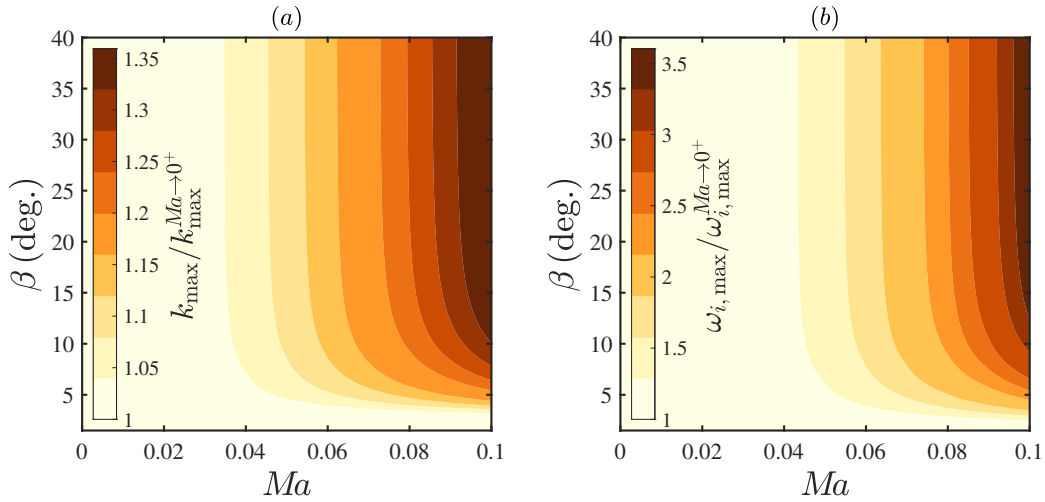


Figure 6: Effect of the Mach number  $Ma = O(\varepsilon)$  and of the angle of inclination  $\beta$  on the stability of a falling water–glycerin film. Deviation of (a) the most unstable wavenumber  $k_{\max}$  from its incompressible limit  $k_{\max}^{Ma \rightarrow 0^+}$ , (b) the maximum growth rate  $\omega_{i, \max}$  from its incompressible limit  $\omega_{i, \max}^{Ma \rightarrow 0^+}$  for a value of Reynolds critical ratio (38) equal to  $\text{RCR} = 1.05$ . In overall terms, darker regions correspond to a greater destabilisation. The set of parameter values and fluid physical properties is the same specified for figure 3.

619 as shown in figures 6a and 5b, indicating that the destabilization involves  
 620 both long and relatively short waves. Meanwhile, the maximum growth rate  
 621  $\omega_{i, \max}$  can reach values up to about three and a half times higher than the  
 622 incompressible one.

623 A method to explore the role of compressibility at highly-tilted config-  
 624 urations consists in predetermining an adequate value of  $Re$ . For such a  
 625 selection, we chose to cover a reasonably broad spectrum of slopes (with  
 626 special attention to the steepest ones), without dropping the shallowness  
 627 assumption.

628 Figure 7 displays the contours of the normalised cut-off wavenumber as

629 a function of the Mach number and of the inclination angle for two different  
 630 fixed values of the Reynolds number, corresponding to (a)  $Re = 1$  (with  $\beta$   
 631 ranging between  $60^\circ$  and  $90^\circ$ ) and (b)  $Re = 3$  (with  $20^\circ \leq \beta \leq 60^\circ$ ). These  
 632 combination of  $(Re, \beta)$  is such as to determine the onset of interfacial in-  
 633 stability. From panels *a-b*, one may erroneously infer that, as  $\beta$  increases,  
 634  $k_c/k_c^{Ma \rightarrow 0^+}$  exhibits a diminishing trend in contrast with previous results.  
 635 However, this evolution is fully justifiable in the following terms: keeping  
 636  $Re$  fixed while the solid substrate steepens is tantamount to moving further  
 637 away from the critical threshold, which corresponds to a progressive aug-  
 638 mentation of the Reynolds critical ratio RCR, that is a situation where the  
 639 compressibility-related effects on the destabilisation are less significant. As  
 640 a consequence, figure 7 is consistent with what displayed in figures 3, 5 and,  
 641 besides, helps in extending our analysis to the case of a vertical falling film  
 642 flow.

643 As final part of the parametric study our sole aim is to investigate the  
 644 influence of the Weber number  $We$  – and thus of the surface tension – on the  
 645 compressibility-induced destabilising mechanism. To do so, we conclude by  
 646 presenting numerical results for three different fluids: (i) water, (ii) aqueous  
 647 solution of dimethylsulfoxide (DMSO), and (iii) aqueous solution of glycerin.  
 648 As summarised in table 1, these fluids display different physical properties  
 649 in terms of density, kinematic viscosity and surface tension, notwithstanding  
 650 that the adopted barotropic EoS (14) remains unaltered among them. As  
 651 regards the other variables belonging to the parameter space, the angle of  
 652 inclination and the Reynolds critical ratio have been kept fixed and equal  
 653 to  $\beta = 15^\circ$  and  $RCR = 1.05$ , respectively. Such a choice corresponds to



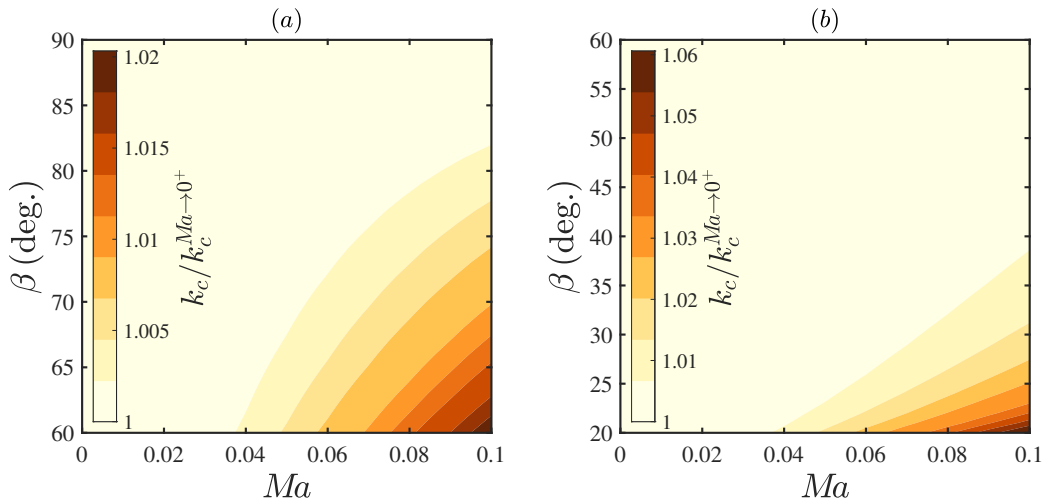


Figure 7: Effect of the Mach number  $Ma = O(\varepsilon)$  and of the angle of inclination  $\beta$  on the stability of a falling water–glycerin film in terms of deviation of the cut–off wavenumber  $k_c$  from its incompressible limit  $k_c^{Ma \rightarrow 0^+}$  with reference to the temporal growth rate of linear disturbances  $k c_i(k)$ , for two different fixed values of the Reynolds number, corresponding to (a)  $Re = 1$  and (b)  $Re = 3$ . In overall terms, darker regions correspond to a greater destabilisation. The set of parameter values and fluid physical properties is the same specified for figure 3.

Fluid	$\tilde{\rho}_0$ (kg m <sup>-3</sup> )	$\tilde{\nu}_0$ (10 <sup>-6</sup> m <sup>2</sup> s <sup>-1</sup> )	$\tilde{\gamma}_0$ (10 <sup>-3</sup> N m <sup>-1</sup> )	$Ka$
Water	1000.0	1.00	76.9	3592
DMSO (83.11%)	1098.3	2.85	48.4	509.5
Glycerin (50%)	1130.0	5.02	69.0	331.8

Table 1: Physical properties of fluids considered in the numerical stability calculations. The working liquids are the same as in Lavalle et al. (2019) (table 3 there): water, an aqueous solution of DMSO at 83.11% by weight, and an aqueous solution of glycerin at 50% by weight. The Kapitza number  $Ka$  is defined as  $Ka = \tilde{\gamma}_0 \left( \tilde{\rho}_0 g^{1/3} \tilde{\nu}_0^{4/3} \right)^{-1}$ , being  $\tilde{\nu}_0 = \tilde{\mu}_0 / \tilde{\rho}_0$  the kinematic viscosity of the fluid under consideration.

654 the following set of values for the Weber number: (i)  $We = 8.841 \cdot 10^{-4}$ , (ii)  
655  $We = 6.234 \cdot 10^{-3}$ , (iii)  $We = 1.156 \cdot 10^{-2}$ . We have represented in figure 8  
656 the cut-off wavenumber (a) and the maximum growth rate (b) as a function  
657 of the Mach number  $Ma$  for the three liquids considered. As before, in  
658 both panels the quantities shown are related to their analogues in the limit  
659 of a perfectly incompressible flow. Within the present weakly compressible  
660 scenario, we see that the onset of the long-wave instability is dimly affected  
661 by surface tension and the destabilising effect of compressibility is felt earlier  
662 at low Weber numbers.

## 663 6. Physical basis for the destabilising effect of compressibility

664 This section aims at clarifying the underlying physics behind the com-  
665 pressibility effect on the onset of the flow primary instability.

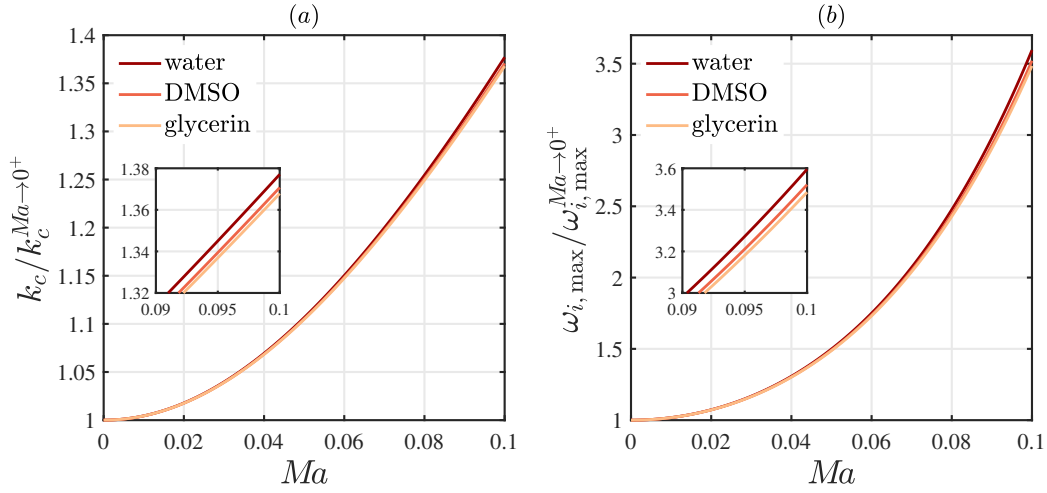


Figure 8: Effect of the Mach number  $Ma = O(\varepsilon)$  on the stability of three falling film flows, each obtained employing one of the fluids detailed in table 1 in terms of physical properties and listed in the legend. Curves represent the deviation of (a) the cut-off wavenumber  $k_c$  from its incompressible limit  $k_c^{Ma \rightarrow 0^+}$  and (b) the maximum growth rate  $\omega_{i, \max}$  from its incompressible limit  $\omega_{i, \max}^{Ma \rightarrow 0^+}$  with reference to the temporal growth rate of linear disturbances  $\omega_i(k) \equiv k c_i(k)$ , for a fixed value of the Reynolds critical ratio (38), equal to  $\text{RCR} = 1.05$ , and inclination angle  $\beta = 15^\circ$ .

666 *6.1. Whitham wave hierarchy*

667 The hydrodynamic stability of a shallow–water flow is linked to the prop-  
 668 agation of interfacial waves (Whitham, 1974; Alekseenko et al., 1985, 1994;  
 669 Ooshida, 1999; Kalliadasis et al., 2013). In this respect, Whitham’s theory  
 670 of two–wave competition serves as a framework to interpret the linear sta-  
 671 bility properties of the depth–averaged weakly–compressible model (25). To  
 672 do so, we can make use of the dispersion relation (32) to study the mech-  
 673 anism at the base of the compressible–induced destabilisation. Specifically,  
 674 we formally recast (32) into the canonical form

$$i (c - c_k) + \Omega k (c - c_{d^+})(c - c_{d^-}) = 0, \quad (39)$$

675 where  $c_k(k^2; Re, \beta, We, Ma)$ ,  $c_{d^\pm}(k^2; Re, \beta, We, Ma)$  and  $\Omega(k^2; Re)$  are de-  
 676 fined as follows

$$c_k = \frac{3}{2k^2 + 3} \left[ 3 + k^2 \left( -1 - \frac{4}{7} Re \cot \beta + \frac{24}{35} Re^2 - \frac{3}{Re} Ma^2 \cot \beta \right) - \frac{4}{21} \frac{Re^2}{We} k^4 \right] \quad (40a)$$

$$c_{d^\pm} = -\frac{9 Ma^2 \cot \beta}{4 Re} \pm \frac{1}{2} \sqrt{\frac{4 k^2}{We} + \frac{12 \cot \beta}{Re} + \frac{108}{5} + \frac{81 Ma^4 \cot^2 \beta}{4 Re^2}} \quad (40b)$$

$$\Omega = \frac{Re}{2k^2 + 3}. \quad (40c)$$

677 Since the dispersion relation (39) recalls a two–wave structure, our reduced  
 678 model (25) can be systematically reinterpreted as a second–order wave equa-  
 679 tion

$$\underbrace{(\partial_t + c_k \partial_x) h}_{(i)} + \Omega \underbrace{(\partial_t + c_{d^-} \partial_x)(\partial_t + c_{d^+} \partial_x) h}_{(ii)} = 0, \quad (41)$$

680 which consists of two levels (i) (ii) of linear hyperbolic wave equations. The  
 681 lower–order solutions to (i) are the *kinematic* waves since they origin from the

682 mass conservation (25a). These fast waves travel at a speed equal to  $c_k$  and  
 683 they are dominant at long time and in the inertia-less limit  $\Omega(Re) \rightarrow 0^+$ .  
 684 Conversely, the higher-order *dynamic* waves of the second kind (ii) arise  
 685 from the film response, governed by the stress continuity condition (10b –  
 686 10c) or – equivalently – by the momentum balance (25b), to variations in  
 687 momentum, hydrostatic pressure and surface tension. They correspond to  
 688 the limit  $\Omega(Re) \rightarrow +\infty$ . In their early stage, wavefronts located at the  
 689 leading front and at the trailing edge of a produced wave packet begin to  
 690 travel at a speed equal to  $c_{d+}$  and  $c_{d-}$ , respectively.

691 Interestingly, the dependence of  $\Omega(k)$  on the wavenumber  $k$  is a mere con-  
 692 sequence of the non-hyperbolicity of the evolution equation appertaining to  
 693 the integral model (25), since terms whose order of spatial derivation exceeds  
 694 the second would be ultimately included in it (Ruyer-Quil, 2012; Kalliadasis  
 695 et al., 2013). Physically, this means that surface wave dispersion is modified  
 696 by the streamwise viscous diffusion as early as the instability onset (Sharma  
 697 and Dandapat, 2006). Anyway,  $\Omega(k^2)$  is not appreciably affected by the  
 698 squared wavenumber  $k^2$ . In fact, by inspection of (40c), the denominator  
 699  $2k^2 + 3 \approx 3$  within the long-wave limit ( $k \ll 1$ ). As an *a posteriori* argu-  
 700 ment, this fact adds legitimacy to the assumption of virtually non-dissipative  
 701 fluid (Samanta et al., 2011), postulated in § 3.1 behind the adoption of (14)  
 702 as barotropic EoS. The dependence (40a) of the kinematic wave speed  $c_k$  on  
 703 the squared wavenumber  $k^2$  gives an estimate of the dispersive role of the  
 704 streamwise second-order viscous terms, sometimes referred to as “viscous  
 705 dispersive effect” (Ruyer-Quil et al., 2008).

706 *6.1.1. Two-wave reframing of the critical threshold*

707 Whitham (1974) proved that the film primary instability can be precisely  
708 reasoned in terms of competition between kinematic and dynamic waves.  
709 Whenever a multi-speed equation of the kind given in (41) holds, long-wave  
710 interfacial disturbances will damp on the condition that kinematic waves  
711 travel at a speed ranging between the speeds of dynamic waves:

$$c_{d-} \leq c_k \leq c_{d+}. \quad (42)$$

712 The origin of the temporal stability criterion (42) stems from the evolution  
713 of a localised precursory ripple (Ruyer-Quil, 2012). Since kinematic waves  
714 tend to emerge from the wave packet at long times, whereas its short-term  
715 dynamics is dominated by dynamic waves, the only stable situation is one  
716 where the back and front of the wave travel at dynamic wave speed  $c_{d-}$  and  
717  $c_{d+}$  respectively, which implies constraint (42). The base state is marginally  
718 stable if  $c_{d-} = c_k$  or  $c_{d+} = c_k$ . Here, in practice, only the latter condition has  
719 a binding character on the inception of the flow instability. Once evaluated  
720 in the limit of infinitely long waves ( $k \rightarrow 0^+$ ), it is verified that equality:

$$c_{d+} = c_k \quad (43)$$

721 is coherently able to recover (36), thus being in line with the expression for  
722 the neutral stability threshold previously found by means of an asymptotic  
723 expansion *à la* Yih (1963) for the wave celerity  $c(k)$ .

724 *6.1.2. Elucidation of the compressibility-induced destabilising effect*

725 To illustrate how compressibility enters Whitham's paradigm, we follow  
726 the methodology adopted by Samanta et al. (2011) and Samanta (2014) for

727 liquid films falling along a slippery incline or in the presence of imposed shear  
 728 stress, respectively. We consider the scenario discussed in figure 4(*a, d*), *i.e.*  
 729 a water–glycerin film down a plane inclined at  $\beta = 1.5^\circ$  and  $\beta = 12^\circ$ . For  
 730 these two angles of inclination, figure 9 compares the kinematic wave speed  
 731  $c_k$  and the dynamic one  $c_{d+}$  given by (40a) and (40b) as a function of the  
 732 squared dimensionless wavenumber  $k^2$ , both within the incompressible limit  
 733  $Ma \rightarrow 0^+$  (solid lines) and in a slightly compressible case, where  $Ma = 0.1$   
 734 (dashed lines). Two values of the Reynolds critical ratio RCR – beyond  
 735 the stability threshold, though in its vicinity – have been examined: (*a, c*)  
 736  $\text{RCR} = 1.025$  and (*b, d*)  $\text{RCR} = 1.075$ .

737 Figure 9 evidences that the compressibility contributes in lowering both  
 738 the dynamic and the kinematic wave speeds. For further clarification, fig-  
 739 ure 9 has been completed with a proper close–up of the plane portion where  
 740 curves cross each other. One easily realizes that each compressible cut–off  
 741 point (void circle) is always located at a higher squared wavenumber  $k^2$  in  
 742 comparison with its incompressible analogue (filled circle).

743 The kinematic wave speed  $c_k$ , however, is much less affected by the com-  
 744 pressibility than the dynamic one  $c_{d+}$ . This can be inspected by a brief dis-  
 745 cussion on the role of inertia. Let us first consider the low–angle configuration  
 746 (upper panels). In such a scenario, the variation in the Reynolds critical ratio  
 747 RCR in figure 9*a, b* seems to only have a minor impact on the compressible  
 748 dynamic celerity  $c_{d+}$  in terms of vertical shift. On the other hand, for the  
 749 greatest RCR (panel *b*), the parabolic–like trend of the kinematic celerity  $c_k$   
 750 evolves with respect to  $k^2$  in such a way that its descending tract gets drasti-  
 751 cally steeper in the vicinity of its point of intersection with the graph of the

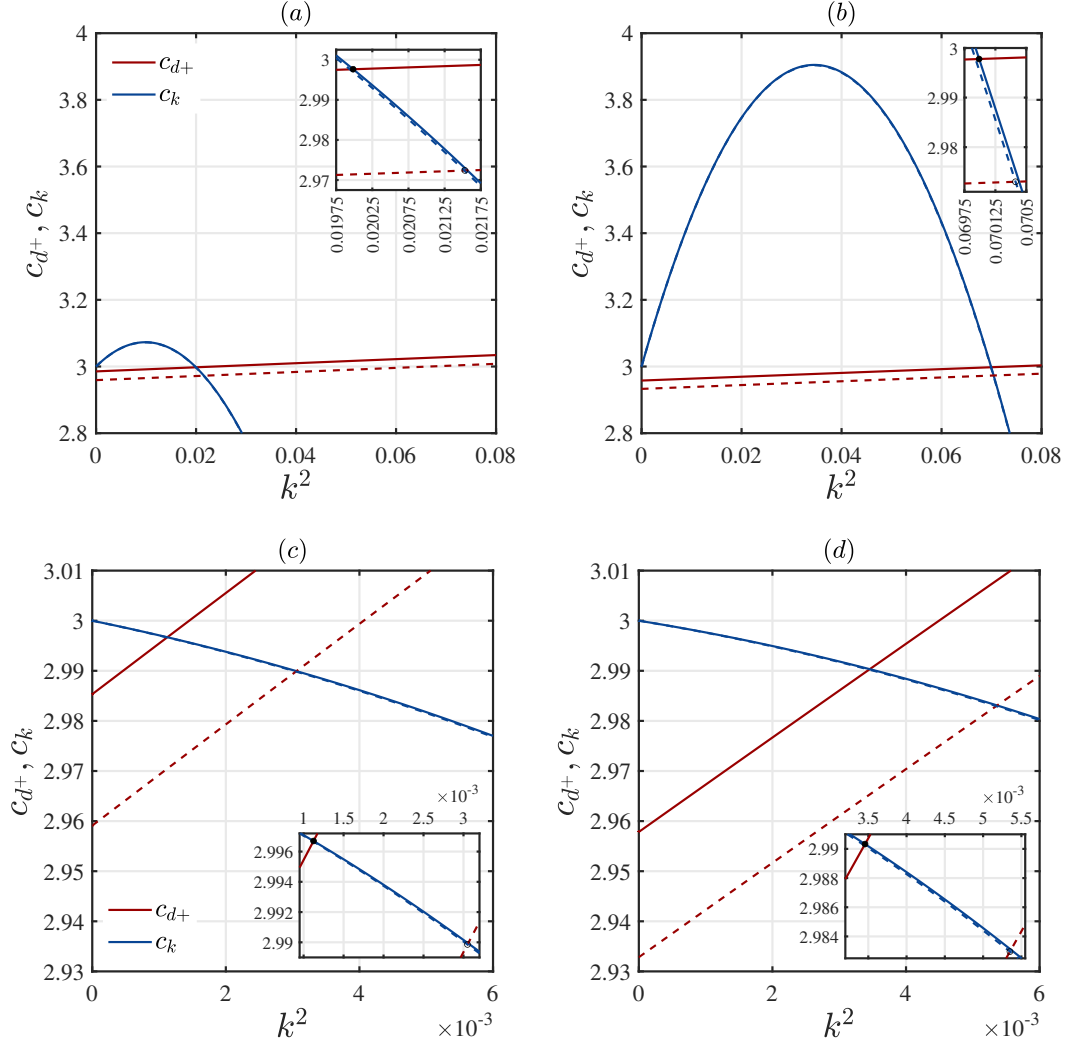


Figure 9: The variation of dynamic  $c_{d+}$  (in red) and kinematic  $c_k$  (in blue) wave speeds as a function of  $k^2$  when the Mach number  $Ma$  passes from zero (solid lines) to a value of 0.1 (dashed lines), for different configurations in terms of angle of inclination  $\beta$  and Reynolds critical ratio RCR. (a-b):  $\beta = 1.5^\circ$ . (c-d):  $\beta = 12^\circ$ . Left panels: RCR = 1.025. Right panels: RCR = 1.075.



752 dynamic wave velocity  $c_{d+}$ . As a consequence, the compressibility-induced  
 753 destabilisation gets noticeably reduced when the Reynolds number increases.

754 We close this section by comparing panels ( $c - d$ ), for which the incli-  
 755 nation angle is  $\beta = 12^\circ$ . Here we notice that the speed of kinematic waves  
 756  $c_k$  is less sensitive in comparison with the previous low-angle configuration  
 757 to the same increase in the Reynolds critical ratio, from  $\text{RCR} = 1.025$  (left)  
 758 to  $\text{RCR} = 1.075$  (right). Meanwhile, the dynamic wave speed  $c_{d+}$ , which  
 759 increases as a straight line with the square of the wavenumber  $k^2$ , under-  
 760 goes deceleration by enhancing compressibility, but also by increasing RCR,  
 761 leading to an attenuation of the compressibility-induced destabilisation.

## 762 6.2. Impact of compressibility on flow-related quantities

763 Aiming at finding a physical source to which the overflow uncovered in  
 764 § 4.1.1 may be attributed, we rephrase the pertinent perturbative analogue  
 765  $\Delta q_{\text{rel}}^{(2)} = (q^{(2)} - q^{(2)}|_{\text{Ma} \rightarrow 0+}) / q^{(0)}$  in terms of dimensional variables, which  
 766 gives:

$$\Delta q_{\text{rel}}^{(2)} = \frac{\Lambda g \tilde{h} \cos \beta}{8 \tilde{a}_0^2}. \quad (44)$$

767 In a similar way, as the leading-order wall shear stress  $\tau_w^{(0)} \equiv \partial_y u^{(0)}|_{y=0}$  is  
 768 employed as normalising quantity for the extra wall shear stress profile, we  
 769 obtain:

$$\Delta \tau_{w, \text{rel}}^{(2)} = \frac{\Lambda g \tilde{h} \cos \beta}{6 \tilde{a}_0^2}. \quad (45)$$

770 The same functional form is manifestly shared by (44) and (45). A simple  
 771 physical interpretation of the ratio therein contained, namely  $g \tilde{h} \cos \beta / \tilde{a}_0^2$ ,  
 772 can be given in the following terms:

$$\Delta q_{\text{rel}}^{(2)}, \Delta \tau_{\text{rel}}^{(2)} \propto \frac{\tilde{\rho} g \tilde{h} \cos \beta}{\tilde{\rho} \tilde{a}_0^2} = \frac{\tilde{P}_{\text{h}}^{\text{eff}}}{\tilde{P}_{\text{a}}}. \quad (46)$$

773 We can notice that (46) accounts for the ratio between the effective com-  
774 ponent of the hydrostatic pressure  $\tilde{P}_h^{\text{eff}}$  exerted along the cross-stream di-  
775 rection by the wavy fluid column of height  $\tilde{h}$ , as stipulated by Stevin’s law,  
776 and a reference acoustic pressure  $\tilde{P}_a$ . As a matter of fact, the whole operat-  
777 ing mechanism through which compressibility acts as a destabilising factor  
778 for the temporal development of long-wave linear disturbances should be  
779 intended as the competition of multiple effects: for decreasing angles of in-  
780 clination, the gravitational effect is emphasised as  $\cos \beta$  increases, but such a  
781 trigger for destabilisation is counterbalanced by the decrease of the uniform  
782 film thickness  $\tilde{h}_N$ , which is a function of  $\sin \beta$ , and so of  $\tilde{h}$ .

783 *6.2.1. Compressible lag of flow rate perturbations*

784 In order to explain the physical mechanism responsible for the compressibility-  
785 induced flow destabilisation, we adapt the basic rationale behind the method-  
786 ology followed by Lavalle et al. (2019) in the context of confined falling liquid  
787 films in presence of an active upper phase. We start by recalling that the  
788 driving mechanism of Kapitza instability can be traced back to inertia, which  
789 is responsible for the time lag between the actual liquid flow rate  $q(h(x, t))$   
790 and its inertialess target value:

$$q^*(h(x, t)) = \underbrace{\frac{\Lambda h^3}{3}}_{q^{*,g}} + \underbrace{\frac{Ma^2 h^4 \Lambda^2 \cot \beta}{8 Re}}_{q^{*,Ma}} + O(\varepsilon^2). \quad (47)$$

791 Here the second-order contribution arising from the flow compressibility has  
792 been highlighted individually, without expressly taking its limit as  $Re \rightarrow 0^+$   
793 owing to its divergent behaviour. Instead, two other  $Re$ -independent second-  
794 order terms contained within the expression of  $q^{(2)}$  and arising in particular

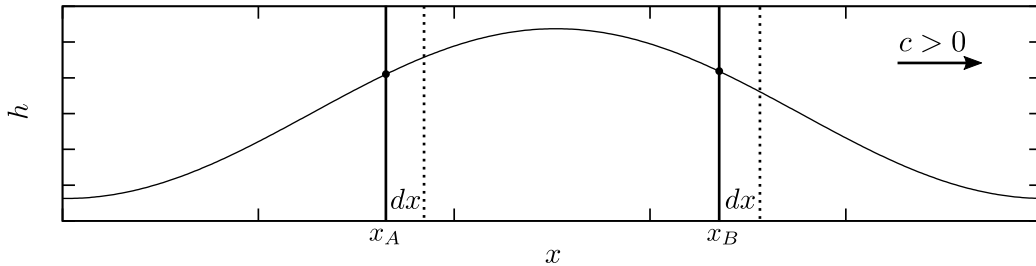


Figure 10: Description scheme of the inertia-based mechanism of the Kapitza instability: by comparison between two points of abscissa  $x_A$  and  $x_B$ , located at opposite sides of a wave peak, the local film flow rate  $q(x, t)$  is delayed in accommodating itself to film thickness variations induced by the passage of the superficial disturbance of speed  $c$ .

795 from the normal stress continuity condition (10b) at order  $O(\varepsilon^2)$  have not  
 796 been explicitly written in (47) and disregarded for simplicity in subsequent  
 797 calculations. Such a decomposition therefore appears to be accurate at  $O(\varepsilon)$   
 798 and it is used only as a means to gain insight at the mechanism at work  
 799 by estimating the relative importance of each individual component in the  
 800 destabilisation of the weakly-compressible flow.

801 The destabilising role of inertia on single-peaked Kapitza waves can be  
 802 explained resorting to the analysis followed by Dietze (2016), who considered  
 803 the history of two points located along the film free-surface either side of a  
 804 wave crest. With reference to figure 10, at the abscissa  $x_B$  upstream of the  
 805 wave hump, where  $\partial_x h < 0$ , the film thickness increases in time as the wave  
 806 covers a distance  $dx$ , and so does the flow rate  $q$  along the  $x$  direction, in  
 807 accordance with Benney's leading-order asymptotic expansion (B.1c). Con-  
 808 versely, at the abscissa  $x_A$  downstream of the wave hump, the film thickness  
 809 and the flow rate decrease when the wave covers  $dx$ . In the presence of in-  
 810ertia, the flow rate cannot adapt instantaneously to such a film thickness

811 variation. As a result, the flow rate in  $x_A$  will be too high while it will be too  
 812 low in  $x_B$ . The ensuing discrepancy in flow across the wave peak accounts  
 813 for its growth. Such a response is more intense as the lag phase of the actual  
 814 flow rate  $q$  behind its target value  $q^*$  increases.

815 According to (47), the effect of gravity through the cubic dependence  
 816 of  $q^{*,g}(h)$  on  $h$  tends to promote variations in  $q^*$  between the wave hump  
 817 and the wave trough as an outcome of the change in film thickness  $h$ . The  
 818 non-negative compressible contribution  $q^{*,Ma}(h)$  exacerbates such an effect,  
 819 increasingly so as the corresponding term in (47) gains relevance. For a per-  
 820 tinent quantification, variables appearing in equation (47), *viz.* the wavy film  
 821 thickness  $h$  and the inertialess film flow rate  $q^*$ , are linearly perturbed around  
 822 the aforesaid (see § 4.1.1) base state vector  $\mathbf{Q}_0$ , via superimposition of  
 823 infinitesimal disturbances of amplitude  $\|\hat{\mathbf{Q}}\| \ll \|\mathbf{Q}_0\|$ :

$$h(x, t) = h_0 + \hat{h}(x, t) \quad (48a)$$

$$q^*(h) = q_0 + \hat{q}(h). \quad (48b)$$

824 By virtue of (48) it is now possible to discriminate between the magnitude  
 825 of perturbations  $\hat{q}^g$  and  $\hat{q}^{Ma}$ , which are, respectively, of gravitational and  
 826 compressible provenance:

$$\hat{q}(\hat{h}) = \underbrace{\Lambda h_0^2 \hat{h}}_{\hat{q}^g} + \underbrace{\frac{Ma^2 h_0^3 \hat{h} \Lambda^2 \cot \beta}{2 Re}}_{\hat{q}^{Ma}}. \quad (49)$$

827 The following expression can be obtained for the so-defined compressible-  
 828 to-total amplitude ratio  $\hat{q}^{Ma}/\hat{q}$ :

$$\left| \frac{\hat{q}^{Ma}}{\hat{q}} \right| = \frac{3 Ma^2 \cot \beta}{2 Re + 3 Ma^2 \cot \beta} \stackrel{(*)}{=} \frac{9 Ma^2}{5 RCR + 9 Ma^2}, \quad (50)$$

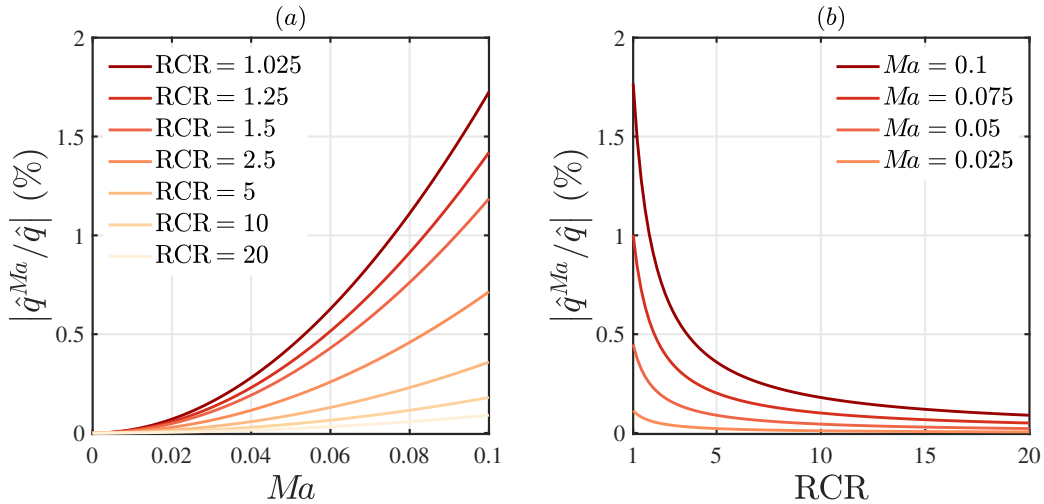


Figure 11: Percentage contribution of the compressibility-related perturbation  $\hat{q}^{Ma}$  to the total inertialess flow rate perturbation  $\hat{q}$  (49) (a) as a function of the Mach number  $Ma = O(\varepsilon)$  for different fixed values of the Reynolds critical ratio RCR (displayed in the legend) and (b) *vice versa*.

829 in which use has been made of the equality  $\Lambda = 3$  and of the identity  $h_0 \equiv 1$ ,  
830 (\*) together with the definition of the Reynolds critical ratio RCR (38), cou-  
831 pled with the incompressible evaluation of the critical threshold  $\lim_{Ma \rightarrow 0^+}$  (36),  
832 in lieu of the Reynolds number  $Re$ . Figure 11 shows that the ratio expressed  
833 by (50) (a) increases with the Mach number  $Ma$  and (b) decreases with the  
834 Reynolds critical ratio RCR, which is in accordance with the most promi-  
835 nent role played by compressibility in the film flow destabilisation shown in  
836 section § 5.

## 837 7. Conclusions

838 Liquid films occur over a wide range of length scales and are central  
839 to numerous areas of pure and applied sciences (Craster and Matar, 2009).

840 The development of long-wave instabilities along its interface leads to self-  
841 excitation of non-trivial dynamics (Sharma and Dandapat, 2006). The mo-  
842 tivation behind this study is addressing theoretically how changes in the  
843 fluid density fit into this context. For such purpose, we have discussed three  
844 guiding questions.

845 (i) How does compressibility affect the structure of a depth-integral model?

846 We considered a barotropic relation involving the Mach number of the mean  
847 flow. Under the assumption of weak compressibility  $Ma \ll 1$ , the density  
848 of the fluid is found to be exponentially stratified against gravity along the  
849 crosswise direction. In the final depth-averaged system (25) this is reflected  
850 in two additional terms: one  $\propto \cot \beta Ma^2/Re$  in the continuity equation, and  
851 the other  $\propto \cot \beta Ma^2/Re^2$  in the momentum conservation equation.

852 (ii) To what extent does compressibility take part in long-wave insta-  
853 bility? According to our linear analysis, a low degree of compressibility  
854 boosts the inception of interfacial instability. This effect is most marked in  
855 low-inertial regimes. For instance, with reference to figure 5*b*, the instabil-  
856 ity threshold of a water-glycerin film flow having  $Re = 2.40$ ,  $\beta = 20^\circ$  and  
857  $Ma = 0.1$  as set of distinctive parameters is seen to increase by 35% in terms  
858 of the cut-off wavenumber with respect to its incompressible analogue. A  
859 higher-order additive correction of the base flow rate, hydrostatic in nature,  
860 has been highlighted via (44). As perspective on future research, the de-  
861 rived depth-integrated model (25) will be also of interest to simulate the  
862 non-linear dynamics of weakly-compressible falling liquid films, on condi-  
863 tion that proper manipulations are performed for the numerical treatment of  
864 capillary terms (Lavalle et al., 2015).

865 (iii) Which is the underlying physical foundation? Albeit of small magni-  
866 tude, differences between the compressible and incompressible nature of the  
867 long-wave instability can be traced back to a compressible-induced deceler-  
868 ation of dynamic waves (figure 9) or, equivalently, to an additional inertia-  
869 induced delay (relative to the kinematic waves) of the flow rate in adapting  
870 to a time-varying film-thickness (figure 11).

### 871 Acknowledgements

872 Authors record their sincerest gratitude for financial support allocated during  
873 the course of this work by the Auvergne-Rhône-Alpes region as part of the  
874 project “MuscaFlow” (21 007147), agreed between Mines Saint-Etienne and  
875 Università di Brescia.

### 876 Declaration of interests

877 The authors report no conflict of interest.

### 878 Appendix A. Reduction of the pressure profile

879 The complete solution of (16) is given by:

$$\begin{aligned}
p(x, y, t; \vartheta) = & p_i + \frac{\overbrace{\exp\left[\frac{\cos\beta}{Fr}Ma^2(h-y)\right]^{-1}}^{\diamond}}{Ma^2} - \frac{\varepsilon^2}{We}\partial_{xx}h + \\
& + \frac{\varepsilon}{Re}\left[\mathcal{W} - \mathcal{W}|_h \overbrace{\exp\left[\frac{\cos\beta}{Fr}Ma^2(h-y)\right]}^{\diamond} - \left(\frac{2}{3} - \vartheta\right)(\partial_x u + \partial_y v)|_h \right. \\
& \left. + 2(\partial_y v)|_h - 2\overbrace{\partial_x h(\partial_y u)|_h}^{\diamond}\right] - \mathcal{I}(y, \mathcal{W}) \exp\left(-\frac{\cos\beta}{Fr}Ma^2 y\right),
\end{aligned}
\tag{A.1}$$

880 where  $\mathcal{I}(y, \mathcal{W})$  is the so-defined primitive

$$\mathcal{I}'(y, \mathcal{W}) = \varepsilon Ma^2 \frac{\cos \beta}{Re Fr} \mathcal{W} \exp\left(\frac{\cos \beta}{Fr} Ma^2 y\right), \quad (\text{A.2})$$

881 the prime mark denoting total differentiation with respect to  $y$ . By inspection  
 882 of (A.2), since it is assumed  $Re \sim Fr = O(1)$ ,  $\mathcal{I}'$  can be regarded as an  
 883  $O(\varepsilon Ma^2)$  residual contribution, originating from the process of integration  
 884 by parts in the context of the application of Duhamel's technique. Given that  
 885 its analytical integration would at least require *a priori* knowledge concerning  
 886 the explicit expression for the unknown spatial derivatives of the velocity field  
 887  $\mathbf{v} = (u, v)$  involved within  $\mathcal{W}$  as part of the integrand function (A.2), we seek  
 888 for a low-compressibility restriction of the kind

$$\varepsilon Ma^2 \lesssim \varepsilon^3, \quad (\text{A.3})$$

889 a condition wherein it is legitimate to consistently ignore its respective con-  
 890 tribution within the ultimate problem (9) via (14). Indeed, assignment (A.3)  
 891 has been formalised in asymptotic terms through the equivalence relation (19),  
 892 with  $\alpha \geq 1$  and  $M = O(1) \in \mathbb{R}_0^+$ . By recalling expansion (20) with (A.3)  
 893 in mind, the  $O(\varepsilon)$ -exponential term denoted as  $\blacklozenge$  can be shortened to the  
 894 unitary value only. Furthermore, starting from the definition of  $\mathcal{W}$  – jointly  
 895 given with (16) – it is straightforward to verify that

$$-\mathcal{W}|_h - \left(\frac{2}{3} - \vartheta\right) (\partial_x u + \partial_y v)|_h + 2 (\partial_y v)|_h \equiv -(\partial_x u)|_h. \quad (\text{A.4})$$

896 Finally, the boundary condition (10c) highlights the fact that  $(\partial_y u)|_h =$   
 897  $O(\varepsilon^2)$ , thereby allowing for the removal of  $\blacklozenge$ , which ultimately contributes  
 898 as an  $O(\varepsilon^3)$  term within (A.1). As a result, (A.1) is consistently tantamount  
 899 to (17).



900 **Appendix B. Asymptotic expansions**

901 *Appendix B.1. Leading order  $O(\varepsilon^0)$*

$$u^{(0)}(h(x, t), y) = -\frac{\Lambda(y^2 - 2hy)}{2} \quad (\text{B.1a})$$

$$v^{(0)}(h(x, t), y) = -\frac{\Lambda(\partial_x h) y^2}{2} \quad (\text{B.1b})$$

$$q^{(0)}(h(x, t)) = \frac{\Lambda h^3}{3} \quad (\text{B.1c})$$

902 The steady-state flat-film solution, corresponding to Nusselt flow (Nusselt,  
 903 1916), can be recovered by substituting unity for  $h$  in equations (B.1). This  
 904 shows that the leading order of Benney's development corresponds to local  
 905 equilibrium.

906 *Appendix B.2. First order  $O(\varepsilon^1)$*

$$u^{(1)}(h(x, t), y) = \frac{Re \varepsilon^2}{We} \partial_{xxx} h \left( hy - \frac{y^2}{2} \right) + \frac{Re \cos \beta}{Fr} \partial_x h \left( -hy + \frac{y^2}{2} \right) +$$

$$+ Re \Lambda^2 \partial_x h \left( \frac{hy^4}{24} - \frac{h^4 y}{6} \right) + Re \Lambda \partial_t h \left( \frac{y^3}{6} - \frac{h^2 y}{2} \right) \quad (\text{B.2a})$$

$$v^{(1)}(h(x, t), y) = \frac{Re \varepsilon^2}{We} \left[ \partial_{4x} h \left( \frac{y^3}{6} - \frac{hy^2}{2} \right) - (\partial_x h) (\partial_{xxx} h) \frac{y^2}{2} \right] +$$

$$+ \frac{Re \cos \beta}{Fr} \left[ \partial_{xx} h \left( -\frac{y^3}{6} + \frac{hy^2}{2} \right) + \partial_x^2 h \frac{y^2}{2} \right] +$$

$$+ Re \Lambda y^2 \left[ \partial_{tx} h \left( -\frac{y^2}{24} + \frac{h^2}{4} \right) + (\partial_t h) (\partial_x h) \frac{h}{2} \right] +$$

$$+ Re \Lambda^2 \left[ \partial_{xx} h \left( -\frac{hy^5}{120} + \frac{h^4 y^2}{12} \right) + \partial_x^2 h \left( -\frac{y^5}{120} + \frac{h^3 y^2}{3} \right) \right] \quad (\text{B.2b})$$

$$\begin{aligned}
u^{(2)}(h(x, t), y) &= \frac{Re^2 \Lambda \varepsilon^2}{We} \partial_{xxxx} h \left( \frac{y^6}{360} - \frac{hy^5}{60} + \frac{h^2 y^4}{12} - \frac{h^3 y^3}{6} + \frac{7h^5 y}{30} \right) + \\
&+ \frac{Re^2 \Lambda \varepsilon^2}{We} \partial_x h \partial_{xxx} h \left( \frac{5hy^4}{12} - \frac{3h^2 y^3}{2} + \frac{17h^4 y}{6} \right) + \\
&+ \frac{Re^2 \Lambda \varepsilon^2}{We} \partial_{xx}^2 h \left( \frac{hy^4}{4} - h^2 y^3 + 2h^4 y \right) + \\
&+ \frac{Re^2 \Lambda \varepsilon^2}{We} \partial_x^2 h \partial_{xx} h \left( \frac{y^4}{2} - 2hy^3 + 4h^3 y \right) + \\
&+ \frac{Re^2 \Lambda \cos \beta}{Fr} \partial_x^2 h \left( -\frac{hy^4}{6} + \frac{h^2 y^3}{2} - \frac{5h^4 y}{6} \right) + \\
&+ \frac{Re^2 \Lambda \cos \beta}{Fr} \partial_{xx} h \left( -\frac{y^6}{360} + \frac{hy^5}{60} - \frac{h^2 y^4}{12} + \frac{h^3 y^3}{6} - \frac{7h^5 y}{30} \right) + \\
&+ \Lambda \partial_{xx} h \left( -\frac{y^3}{3} - \frac{hy^2}{2} + \frac{5h^2 y}{2} \right) + \\
&+ Re^2 \Lambda^3 \partial_{xx} h \left( -\frac{hy^8}{4480} + \frac{h^2 y^7}{560} - \frac{h^3 y^6}{180} + \frac{h^4 y^5}{120} + \frac{h^5 y^4}{72} - \frac{h^6 y^3}{18} + \frac{29h^8 y}{315} \right) + \\
&+ Re^2 \Lambda^3 \partial_x^2 h \left( -\frac{y^8}{4480} + \frac{hy^7}{560} - \frac{7h^2 y^6}{720} + \frac{h^3 y^5}{30} + \frac{5h^4 y^4}{72} - \frac{h^5 y^3}{3} + \frac{38h^7 y}{63} \right) + \\
&+ \Lambda \partial_x^2 h \left( 5hy - \frac{y^2}{2} \right) + \frac{M^2 \Lambda \cos \beta}{Fr} \left( \frac{y^3}{6} - \frac{hy^2}{2} + \frac{h^2 y}{2} \right)
\end{aligned} \tag{B.3}$$

913 **Appendix C. Validation with Orr–Sommerfeld problem within the**  
914 **incompressible limit**

915 Our second–order model (25) correctly recovers the expressions for  $c^{(0)}$ ,  $c^{(1)}|_{Ma \rightarrow 0^+}$   
916 and  $c^{(2)}|_{Ma \rightarrow 0^+}$ , which show accordance with the asymptotic expansions of  
917 solutions to Orr–Sommerfeld boundary–value problem – reported in Ruyer–  
918 Quil and Manneville (1998). However, it is expected that higher–order ex-

$Re \cot^2 \beta$	$Re^2 \cot \beta$	$\cot \beta$	$Re/We$	$Re^3$	$Re$
-16.7	21.6	-63.0	0	28.9	7.8

Table C.2: Percent errors [%] (expressed to one decimal place) committed by the incompressible evaluation of the present second-order model (25) $_{|Ma \rightarrow 0^+}$  in the estimate of polynomial coefficients  $\star$  of the  $O(k^3)$  incompressible wave celerity  $c^{(3)}_{|Ma \rightarrow 0^+}$ , given by (34d) $_{|Ma \rightarrow 0^+}$  by comparison with the exact ones (Ruyer-Quil and Manneville, 1998; Chang and Demekhin, 2002) provided by the Orr-Sommerfeld theory.

919 pressions of  $c^{(j)}$  with  $j > 2$  are not correctly captured. Specifically, when the  
920 incompressible limit of  $c^{(3)}$ , expressed by (34d) $_{|Ma \rightarrow 0^+}$ , is contrasted with its  
921 exact Orr-Sommerfeld (O-S) analogue, we notice that all terms are present,  
922 but with different numerical coefficients in front of them in almost every oc-  
923 currence  $\star$ . As shown in table C.2, such discrepancies can be quantified in  
924 terms of relative percentage deviation

$$\frac{\star_{(34d)}^{(3)}_{|Ma \rightarrow 0^+} - \star_{O-S}^{(3)}}{\star_{O-S}^{(3)}} \cdot 100\% \quad [\%]. \quad (C.1)$$

925 A numerical validation of the present second-order weakly-compressible  
926 model within its incompressible limit (25) $_{|Ma \rightarrow 0^+}$  can be accomplished by  
927 comparing its predictions to data from the literature concerning the long-  
928 wave interfacial instability for a liquid falling film flow. Figure C.12 com-  
929 pares growth rate and angular frequency of linear surface waves with results  
930 of Brevdo et al. (1999) for the case of a liquid film falling down an incline  
931 within a passive atmosphere. We remark that agreement is achieved between  
932 the two sets of data with reference to the immediate proximity to the limit of  
933 infinitely long-wave ( $k \rightarrow 0^+$ ), as long as the Reynolds number  $Re$  is chosen

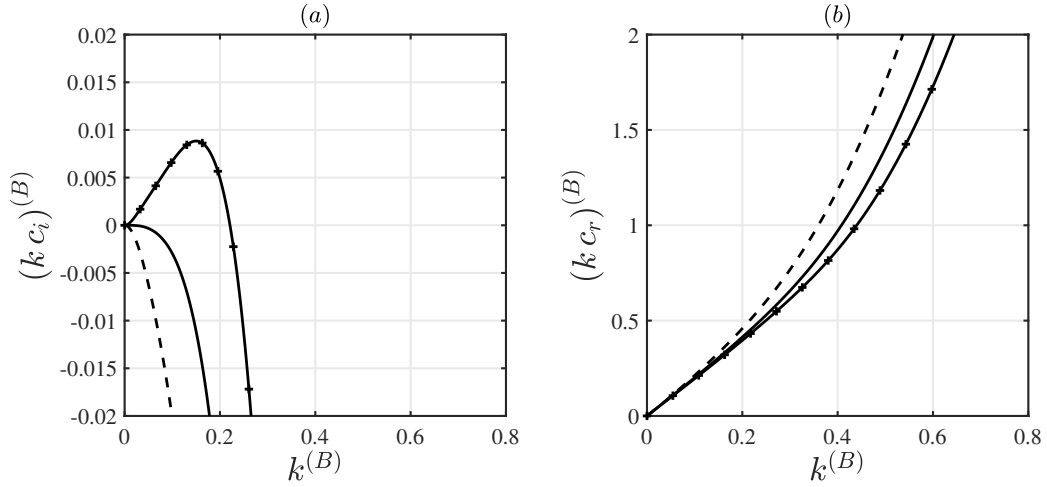


Figure C.12: Comparison of the dimensionless (a) temporal growth rate  $k c_i(k)$  and (b) angular wave frequency  $k c_r(k)$  between our work and Brevdo et al. (1999) (figure 2 there). Parameter values:  $g = 9.81 \text{ m s}^{-2}$ ,  $\beta = 4.6^\circ$ ,  $\tilde{\rho}_0 = 1130 \text{ kg m}^{-3}$ ,  $\tilde{\mu}_0 = 5.673 \cdot 10^{-3} \text{ Pa s}$ ,  $\tilde{\gamma}_0 = 69.0 \cdot 10^{-3} \text{ N m}^{-1}$ . Values of the Reynolds number  $Re^{(B)} = (3/2) Re$  according to Brevdo's scaling: 10 (dashed line),  $Re_{cr}^{(B)} = (5/4) \cot \beta$  (bare solid line), 20 (pluses). Note that  $k^{(B)}$ ,  $(k c_r)^{(B)}$  and  $(k c_i)^{(B)}$  are scaled as in Brevdo et al. (1999), *i.e.* using the Nusselt film thickness  $\tilde{h}_N$  and the free-surface velocity  $(3/2) \tilde{U}_N$  as length and velocity scales, respectively, instead of the film mean velocity  $\tilde{U}_N$  as done here.

934 to be compliant with the pertinent assumption  $Re = O(1)$  made in § 3.

935 **References**

936 Alekseenko, S., Nakoryakov, V., Pokusaev, B., 1985. Wave formation on  
937 vertical falling liquid films. *International Journal of Multiphase Flow* 11,  
938 607–627. doi:10.1016/0301-9322(85)90082-5.

939 Alekseenko, S., Nakoryakov, V., Pokusaev, B., 1994. Wave flow of liquid  
940 films. Begell house.

941 Almqvist, A., Burtseva, E., Pérez-Ráfols, F., Wall, P., 2019. New insights  
942 on lubrication theory for compressible fluids. *International Journal of En-*  
943 *gineering Science* 145, 103170. doi:10.1016/j.ijengsci.2019.103170.

944 Batchelor, G., 2000. *An Introduction to Fluid Dynamics*. Cam-  
945 *bridge Mathematical Library*, Cambridge University Press.  
946 doi:10.1017/CBO9780511800955.

947 Benjamin, T., 1957. Wave formation in laminar flow down an inclined plane.  
948 *Journal of Fluid Mechanics* 2, 554–573. doi:10.1017/S0022112057000373.

949 Benney, D., 1966. Long waves on liquid films. *Journal of Mathematics and*  
950 *Physics* 45, 150–155. doi:10.1002/sapm1966451150.

951 Bresch, D., Cellier, N., Couderc, F., Gisclon, M., Noble, P., Richard, G.L.,  
952 Ruyer-Quil, C., Vila, J.P., 2020. Augmented skew-symmetric system for  
953 shallow-water system with surface tension allowing large gradient of den-  
954 sity. *J. Comput. Phys.* 419, 109670. doi:10.1016/j.jcp.2020.109670.

955 Brevdo, L., Laure, P., Dias, F., Bridges, T.J., 1999. Linear pulse structure

956 and signalling in a film flow on an inclined plane. *J.Fluid Mech.* 396, 37–71.  
957 doi:10.1017/S0022112099005790.

958 Cellier, N., Ruyer-Quil, C., 2020. A new family of reduced models for non-  
959 isothermal falling films. *International Journal of Heat and Mass Transfer*  
960 154, 119700. doi:10.1016/j.ijheatmasstransfer.2020.119700.

961 Chang, H.C., 1986. Nonlinear waves on liquid film surfaces - i. flood-  
962 ing in a vertical tube. *Chemical Engineering Science* 41, 2463–2476.  
963 doi:10.1016/0009-2509(86)80032-x.

964 Chang, H.C., 1994. Wave evolution on a falling film. *Annual Review of Fluid*  
965 *Mechanics* 26, 103–136. doi:10.1146/annurev.fl.26.010194.000535.

966 Chang, H.C., Demekhin, E., 2002. *Complex Wave Dynamics on Thin Films*.  
967 Elsevier.

968 Colinet, P., Legros, J.C., Velarde, M.G., 2001. Nonlinear dynamics of surface-  
969 tension-driven instabilities. volume 527. Wiley Online Library.

970 Craster, R.V., Matar, O.K., 2009. Dynamics and stability of thin liquid films.  
971 *Rev. Mod. Phys.* 81, 1131–1198. doi:10.1103/RevModPhys.81.1131.

972 Dietze, G.F., 2016. On the kapitza instability and the generation of capillary  
973 waves. *J. Fluid Mech.* 789, 368–401. doi:10.1017/jfm.2015.736.

974 Frisk, D.P., Davis, E.J., 1972. The enhancement of heat transfer by waves in  
975 stratified gas–liquid flow. *International Journal of Heat and Mass Transfer*  
976 15, 1537–1552. doi:10.1016/0017-9310(72)90009-9.

- 977 Gjevik, B., 1970. Occurrence of finite-amplitude surface waves on falling  
978 liquid films. *Physics of Fluids* 13, 1918. doi:10.1063/1.1693186.
- 979 Jeffreys, H., 1926. XVI. On the relation to physics of the notion of con-  
980 vergence of series. *The London, Edinburgh, and Dublin Philosophical*  
981 *Magazine and Journal of Science* 2, 241–244.
- 982 Kalliadasis, S., Ruyer-Quil, C., Scheid, B., Velarde, M., 2013. *Falling Liquid*  
983 *Films*. Springer.
- 984 Kapitza, P.L., 1948. Wave flow of thin layers of a viscous fluid: I. free flow.,  
985 in: Haar, D.T. (Ed.), *Collected Papers of P. L. Kapitza (1965)*. Pergamon,  
986 pp. 662–679. (Original paper in Russian: *Zh. Ekper. Teor. Fiz.*, 18, I.  
987 3–18).
- 988 Kapitza, P.L., Kapitza, S.P., 1949. Wave flow of thin fluid layers of liquid., in:  
989 Haar, D.T. (Ed.), *Collected Papers of P. L. Kapitza (1965)*. Pergamon, pp.  
990 662–679. (Original paper in Russian: *Zh. Ekper. Teor. Fiz.*, 19: 105–120).
- 991 Kelly, R.E., Goussis, D.A., Lin, S.P., Hsu, F.K., 1989. The mechanism for  
992 surface wave instability in film flow down an inclined plane. *Phys. Fluids*  
993 *A* 1, 819–826.
- 994 Kinsler, L., Frey, A., Coppens, A., Sanders, J., 2000. *Absorption and Attenuation of Sound*. John Wiley & Sons, New York. p. 210–245.
- 996 Lavallo, G., Li, Y., Mergui, S., Grenier, N., Dietze, G.F., 2019. Suppression  
997 of the kapitza instability in confined falling liquid films. *J. Fluid Mech.*  
998 860, 608–639. doi:10.1017/jfm.2018.902.

- 999 Lavallo, G., Vila, J.P., Blanchard, G., Laurent, C., Charru, F., 2015. A  
1000 numerical reduced model for thin liquid films sheared by a gas flow. *Journal*  
1001 *of Computational Physics* 301, 119–140. doi:10.1016/j.jcp.2015.08.018.
- 1002 Lavallo, G., Vila, J.P., Lucquiaud, M., Valluri, P., 2017. Ultraefficient re-  
1003 duced model for countercurrent two-layer flows. *Phys. Rev. Fluids* 2,  
1004 014001. doi:10.1103/PhysRevFluids.2.014001.
- 1005 Lin, S., 1974. Finite amplitude side-band stability of a viscous film. *Journal*  
1006 *of Fluid Mechanics* 63, 417–429. doi:10.1017/s0022112074001704.
- 1007 Liu, J., Gollub, J., 1994. Solitary wave dynamics of film flows. *Physics of*  
1008 *Fluids* 6, 1702–1712. doi:10.1063/1.868232.
- 1009 Lu, H., Ma, X., Huang, K., Fu, L., Azimi, M., 2020. Carbon dioxide transport  
1010 via pipelines: A systematic review. *Journal of Cleaner Production* 266,  
1011 121994. doi:10.1016/j.jclepro.2020.121994.
- 1012 Meliga, P., Sipp, D., Chomaz, J.M., 2010. Effect of compressibility on the  
1013 global stability of axisymmetric wake flows. *Journal of Fluid Mechanics*  
1014 660, 499–526. doi:10.1017/S002211201000279X.
- 1015 Noble, P., Vila, J.P., 2013. Thin power-law film flow down an inclined plane:  
1016 consistent shallow-water models and stability under large-scale perturba-  
1017 tions. *Journal of Fluid Mechanics* 735, 29–60. doi:10.1017/jfm.2013.454.
- 1018 Noble, P., Vila, J.P., 2014. Stability theory for difference approximations of  
1019 euler–korteweg equations and application to thin film flows. *SIAM Journal*  
1020 *on Numerical Analysis* 52, 2770–2791. doi:10.1137/130918009.



- 1021 Nusselt, W., 1916. Die oberflächenkondensation des wasserdampfes. Z.  
1022 Verein. Deutsch. Ing. 50, 541–546.
- 1023 Ooshida, T., 1999. Surface equation of falling film flows with moderate  
1024 Reynolds number and large but finite Weber number. Physics of Fluids  
1025 11, 3247–3269. doi:10.1063/1.870186.
- 1026 Orr, W.M., 1907. The stability or instability of the steady motions of a  
1027 perfect liquid and of a viscous liquid. part ii: a viscous liquid. Proc. Roy.  
1028 Irish Acad. 27, 69–138. doi:10.2307/20490591.
- 1029 Richard, G., 2021. An extension of the boussinesq-type models to weakly  
1030 compressible flows. European Journal of Mechanics - B/Fluids 89, 217–  
1031 240. doi:10.1016/j.euromechflu.2021.05.011.
- 1032 Richard, G., Gisclon, M., Ruyer-Quil, C., Vila, J., 2019. Optimization of  
1033 consistent two-equation models for thin film flows. European Journal of  
1034 Mechanics - B/Fluids 76, 7–25. doi:10.1016/j.euromechflu.2019.01.004.
- 1035 Richard, G., Ruyer-Quil, C., Vila, J., 2016. A three-equation model for thin  
1036 films down an inclined plane. Journal of Fluid Mechanics 804, 162–200.  
1037 doi:10.1017/jfm.2016.530.
- 1038 Ruyer-Quil, C., 2012. Instabilities and modeling of falling film flows. Fluids  
1039 mechanics [physics.class-ph], Université Pierre et Marie Curie - Paris VI.  
1040 p. 285. URL: <https://theses.hal.science/tel-00746483>.
- 1041 Ruyer-Quil, C., Manneville, P., 1998. Modeling film flows down  
1042 inclined planes. The European Physical Journal B 6, 277–292.  
1043 doi:10.1007/s100510050550.

- 1044 Ruyer-Quil, C., Manneville, P., 2000. Improved modeling of flows  
1045 down inclined planes. *The European Physical Journal B* 15, 357–369.  
1046 doi:10.1007/s100510051137.
- 1047 Ruyer-Quil, C., Manneville, P., 2002. Further accuracy and convergence  
1048 results on the modeling of flows down inclined planes by weighted-residual  
1049 approximations. *Physics of Fluids* 14, 170–183. doi:10.1063/1.1426103.
- 1050 Ruyer-Quil, C., Treveleyan, P., Giorgiutti-Dauphiné, F., Duprat, C., Kalli-  
1051 adasis, S., 2008. Modelling film flows down a fibre. *J. Fluid Mech.* 603,  
1052 431—462. doi:10.1017/S0022112008001225.
- 1053 Samanta, A., 2014. Shear-imposed falling film. *Journal of Fluid Mechanics*  
1054 753, 131–149. doi:10.1017/jfm.2014.351.
- 1055 Samanta, A., Ruyer-Quil, C., Goyeau, B., 2011. A falling film down  
1056 a slippery inclined plane. *Journal of Fluid Mechanics* 684, 353–383.  
1057 doi:10.1017/jfm.2011.304.
- 1058 Shapiro, A.H., 1953. *The Dynamics and Thermodynamics of Compressible*  
1059 *Fluid Flow*. volume 1. John Wiley & Sons, New York.
- 1060 Sharma, A., Dandapat, B.S., 2006. *Wave Dynamics and Stability of Thin*  
1061 *Film Flow Systems*. Alpha Science Int’l Ltd.
- 1062 Shkadov, V.Y., 1967. Wave flow regimes of a thin layer of viscous fluid  
1063 subject to gravity. *Izv. Akad. Nauk SSSR Mekh. Zhidk. Gaza* 1, 43–51.  
1064 doi:10.1007/bf01024797. (translation in 1970 *Fluid Dyn.* **2**, 29–34).

- 1065 Simmonds, J.G., Mann Jr, J.E., 1998. A first look at perturbation theory.  
1066 Courier Corporation.
- 1067 Smith, M.K., 1990. The mechanism for the long-wave instability in thin  
1068 liquid films. *J. Fluid Mech.* 217, 469–485.
- 1069 Sommerfeld, A., 1908. Ein beitrag zur hydrodynamischen erklärung der tur-  
1070 bulenten flussigkeitsbewegung. *Atti Congr. Int. Math.* 4th .
- 1071 Thompson, A.B., Gomes, S.N., Denner, F., Dallaston, M.C., Kalliadasis,  
1072 S., 2019. Robust low-dimensional modelling of falling liquid films sub-  
1073 ject to variable wall heating. *Journal of Fluid Mechanics* 877, 844–881.  
1074 doi:10.1017/jfm.2019.580.
- 1075 Trevelyan, P.M.J., Scheid, B., Ruyer-Quil, C., Kalliadasis, S., 2007.  
1076 Heated falling films. *Journal of Fluid Mechanics* 592, 295–334.  
1077 doi:10.1017/S0022112007008476.
- 1078 Van Dael, W., 1968. *Thermodynamic Properties and the Velocity of Sound.*  
1079 Springer US, Boston, MA. pp. 527–577. doi:10.1007/978-1-4899-6569-1-17.
- 1080 Van Dyke, M., Rosenblat, S., 1975. *Perturbation method in fluid mechanics.*  
1081 The Parabolic Press.
- 1082 Weinstein, S.J., Ruschak, K.J., 2004. Coating flows. *Annu. Rev. Fluid Mech.*  
1083 36, 29–53. doi:10.1146/annurev.fluid.36.050802.122049.
- 1084 Whitham, G., 1974. *Linear and Nonlinear Waves.* Wiley–Interscience.
- 1085 Yih, C.S., 1963. Stability of liquid flow down an inclined plane. *Physics of*  
1086 *Fluids* 6, 321. doi:10.1063/1.1706737.